Contact poling of RKTP with silicon needles

Hoda Kianirad

Master of Science Thesis

Laser Physics

Department of Applied Physics

School of Engineering Science

Royal Institute of Technology

Stockholm, Sweden 2013

به پدر و مادرم

Abstract

Quasi-phase-matching (QPM) is a method to get efficient and tailored second-order nonlinear interactions. Several techniques exist for fabrication of periodic domain structures in ferroelectric crystals for QPM- based frequency conversion. By far, electric field-poling using lithographically patterned electrodes on the z-face of the crystal is the most common one. High-quality, periodically inverted ferroelectric domain structures in flux-grown $KTiOPO_4$ (KTP) crystals were fabricated already in the late 90's using this technique. It has been shown that a slight Rb doping of the KTP crystal (RKTP) facilitates the periodic poling. However, fabrication of two-dimensional (2D) domain structures in RKTP has not yet been investigated. A disadvantage with the lithographic patterning is that each sample needs to be patterned individually, which is tedious and time consuming. Moreover, when it comes to small domain features, which are required by the next generation of nonlinear optical devices, a more versatile poling technique has to be developed due to the limitations of conventional photolithography.

In this work, we present a new technique for 2D domain inversion in a 1 mm thick RKTP crystal and demonstrate the densest 2D lattice in a KTP isomorph. First, 2D periodic arrays of silicon spikes with 20 μm periods and silicon pillars with 5 μm periods were constructed using isotropic dry etching. Second, the silicon arrays were used as a contact electrode in order to periodically pole the RKTP crystal. A 2D domain pattern with 20×20 μm^2 and 5×5 μm^2 periods were obtained. A high normalized conversion efficiency of 1.27 % W^{-1}cm^{-1} was obtained for frequency doubling of a CW Ti-Sapphire laser at 894 nm for the 5 μm period pattern. The measured temperature bandwidth was 4.25 ℃, from which we estimated an effective crystal length of 5.4 mm, which is very close to the physical structure length of 6 mm.

This novel poling technique has several advantages. First, the silicon electrode is reusable and there is no need for patterning each sample individually. Second, the crystalline structure of silicon provides high accuracy and reproducibility in the electrode fabrication. Finally, Si array electrodes can be designed for any desirable period or electrode geometry. Therefore, contact electrode poling with this technique can be a more convenient, flexible, and suitable method for making small feature domain patterns, and it also can reduce the fabrication costs.

Acknowledgment

This work could have never been done alone and without technical and emotional support of several people and I express my gratitude to all of them.

First, Andrius Zukauskas, I would like to thank you for your supervision. Thank you for teaching me all the small theoretical details, how to work in the lab and always having time to answer my questions regarding the experiments and other things. On top of that, thank you for helping me to present my work and guiding me in writing the report.

I would like to gratefully acknowledge the supervision of Thomas Frisk in the fabrication part of my project. Thank you for providing me with knowledge, teaching me your skills and being abundantly helpful. You have given me the chance to work independently and to believe in myself by happily guiding me through this path of life with all the small hints about everything.

I am deeply grateful to Prof. Fredrik Laurell and Carlota Canalias, not only for letting me work on the fascinating and interesting subject of nonlinear optics but also for generously giving me an unlimited access to every instrument and facility that I needed, trusting me in all different parts of my project and willing to discuss my problems at any time. Most importantly, thank you for letting me be a part of Laser physics family, you inspired me to find my passion for research.

I would like to express my thanks of gratitude to Niclas Roxhed for the ICP machine recipe, Jens A. Tellefsen, Jr for proofreading this thesis and for the great guides about writing, Charlotte Liljestrand, for introducing the laser physics group to me, Katia Gallo for all the late night laughs and good portions of food and Arezoo Ghanadian for being a wonderful office mate with all the laughters that made late night work much more fun.

I wish to thank all the members of Laser physics research group for happily sharing their knowledge, giving me hope and help when my mind got stuck, for all the laughters during lunch times and for making me feel so welcome in the group.

I am grateful to all my friends, most importantly to Mandana and Saeed for being the surrogate family during these years of living in Sweden and for their continued love and support thereafter.

Of course, I would like to thank my family for their support through these years of my education. Thank you for believing in me, for your unconditional love that made the physical distance unnoticeable. A special thanks to my parents for their full support in many different ways.

Contents

1 Introduction

1.1 Background

Nonlinear frequency conversion is a very attractive method for achieving coherent radiation in spectral regions inaccessible by available lasers, leading to potential applications ranging from optical communication, spectroscopy and remote sensing, projectors, material processing to diagnostic and medical treatment. Many applications of frequency conversion are based on second-order nonlinear effects utilizing the $\chi^{(2)}$ component of the susceptibility tensor, which is a characteristic of non-centrosymmetric materials, such as lithium niobate (LN), potassium titanyl phosphate (KTP), lithium tantalate (LT), etc. These nonlinear materials have relatively high nonlinear coefficients and are useful for applications such as second harmonic generation (SHG), optical parametric oscillation (OPO), and optical parametric amplification (OPA).

Due to dispersion in the material, incident and generated waves with different wavelengths travel at different velocities and become out of phase, thus reducing the conversion efficiency. For efficient frequency conversion, it is necessary to maintain the phase match between the interacting wavelengths, i.e. , to transfer the energy to the generated wave, the relative phase of the interacting waves must be kept constant. Quasi-phase matching (QPM) brings the interacting waves into phase by adding an artificial momentum vector. The artificial momentum vector in QPM originates from a periodic QPM structure. By periodically inverting the polarization vector, the sign of the $\chi^{(2)}$ susceptibility can be altered and the accumulated phase mismatch between the interacting waves is reset. Changing the polarization locally in ferroelectric material to achieve QPM is called ferroelectric domain engineering or periodic poling. With this technique it is possible to phase-match any conversion in the transparency range of the nonlinear crystal, usually from mid-infrared to near ultra-violet.

There are many different techniques for achieving polarization switching in ferroelectric materials, including chemical treatment, modulation of the sign of the nonlinearity during the ferroelectric crystal growth, electron beam lithography and electric field poling. The latter is the most common technique, which is implemented by applying an electric field periodically over every coherent-length of the interaction in the ferroelectric material. Conventional electric-field poling relies on the creation of periodic electrodes via contact photolithography, limiting the domain size to 1 μm. The lithography process for patterning micro-structured electrodes on each crystal is a complicated and time consuming procedure. The width of the domain-inverted regions with this technique is always larger than that of the initially deposited electrode region. This effect is called domain broadening and it influences the accuracy of the duty cycle. Domain broadening is due to the tangential component of the electric field which results in polarization reversal under the photoresist isolating layer [1]. In order to improve the in-

verted domain grating quality and compensate for the domain broadening, it has been proposed to pattern the metal electrodes with less duty cycle [2]. Hence, in the case of a large wavevector mismatch the QPM structure needs to be in the scale of sub-micron. This corresponds to sub-micron electrode dimensions for small domain pattern grating which is hard to achieve by the photolithography process.

Latest efforts to reduce the domain size to sub-micron scale with less domain broadening include 1) periodic poling of KTP crystal with 720 nm period for backward second harmonic generation [3], 2) poling of Rb-doped KTP (RKTP) crystal with 690 nm period [4], and 3) fabrication of periodically poled KTP (PPKTP) crystals with 800 nm period for mirrorless optical parametric oscillation [5] , [6]. In order to simplify the poling process and to speed up the fabrication procedure, etched Si stamper electrode with 3 µm period has been investigated as an alternative electrode for formation of 1D domains by contact poling in $LiNbO_3$ [7]. However, these electrodes were fabricated by wet etching and the sample thickness was limited to ~200 µm.

1.2 Objective of the work

The aim of this thesis is to investigate a new technique for ferroelectric domain engineering on the micron scale which can reduce the domain broadening as well as the complexity and lithography problems of the conventional technique. In this approach an array of silicon needles is used as a periodic electrode for applying voltage over the crystal in a periodic fashion. To explore the feasibility of this technique, two-dimensional gratings with different periodicity are fabricated as silicon needles on a p-type silicon wafer. This silicon array of needles is used to create two-dimensional domain structures in RKTP crystal. Reproducing the grating structure of the silicon electrode with high accuracy on a crystal can lead to new achievements in periodic poling technique and new applications of quasi-phase matched devices. Finally, the ferroelectric domain structures, poled with silicon electrodes, were analyzed and the optical performance of periodically poled crystals was evaluated.

2 Nonlinear optics

In classical optics the light-matter interaction induces oscillating dipoles with the frequency of the incoming light. Nonlinear optics is the field of optics that studies the interaction of light with matter in the regime where the response of the material to the electromagnetic radiation is nonlinear and depends on the electric field amplitude of the radiation. If the power of the incoming light is high enough, the properties of the material become dependent on the intensity of the illumination. The induced oscillating dipoles create photons with frequencies that are not present in the incoming light. In the first nonlinear-optical experiment of the laser era which was performed by Franken *et al* in 1961, a ruby laser radiation with a wavelength of 694.2 nm was used to generate the second harmonic in a quartz crystal at a wavelength of 347.1 nm [8]. This work was followed by the discovery of a rich diversity of nonlinear optical effects [9]. Therefore, in order to describe frequency conversion, it is necessary to understand the principles of nonlinear optics. In this Chapter, the physics behind the nonlinear frequency conversion will be discussed.

2.1 Linear and nonlinear polarization

When an electromagnetic wave passes through a dielectric medium, the electric field induces a polarization in the material. For low intensity electromagnetic waves, the material response can be approximated in the following way:

$$\widetilde{P}(t) = \epsilon_0 \chi^{(1)} \widetilde{E}(t), \qquad (2.1)$$

where ϵ_0 is the permittivity of the vacuum and $\widetilde{E}$ is the electric component of the electromagnetic wave. This equation shows a linear dependence of the polarization $\widetilde{P}$ on the electric field with a proportionality factor $\chi^{(1)}$ (first order susceptibility), which applies to the linear optical phenomena. When it comes to more intense electromagnetic waves, Eq.(2.1) can be extended to:

$$\widetilde{P}(t) = \epsilon_0 \left[\chi^{(1)} \widetilde{E}(t) + \chi^{(2)} \widetilde{E}^2(t) + \chi^{(3)} \widetilde{E}^3(t) + \cdots \right], \qquad (2.2)$$

or

$$\widetilde{P}(t) = \widetilde{P}^{(1)} + \widetilde{P}^{(2)} + \widetilde{P}^{(3)} + \cdots. \qquad (2.3)$$

The parameters $\chi^{(2)}$ and $\chi^{(3)}$ in Eq.(2.2) are the second and third order susceptibilities, respectively. Regarding the linear and the nonlinear components, Eq.(2.3) can be written as:

$$\widetilde{P}(t) = \widetilde{P}^{L} + \widetilde{P}^{NL}. \qquad (2.4)$$

If the nonlinear part of the induced polarization is strong enough, the oscillating dipoles inside the material emit photons with other frequencies [10].

2.2 Second order nonlinear processes

The term $\epsilon_0 \chi^{(2)} \widetilde{E}^2(t)$ in Eq.(2.2) describes the second order nonlinear interactions, which are illustrated in Fig.(2.1).
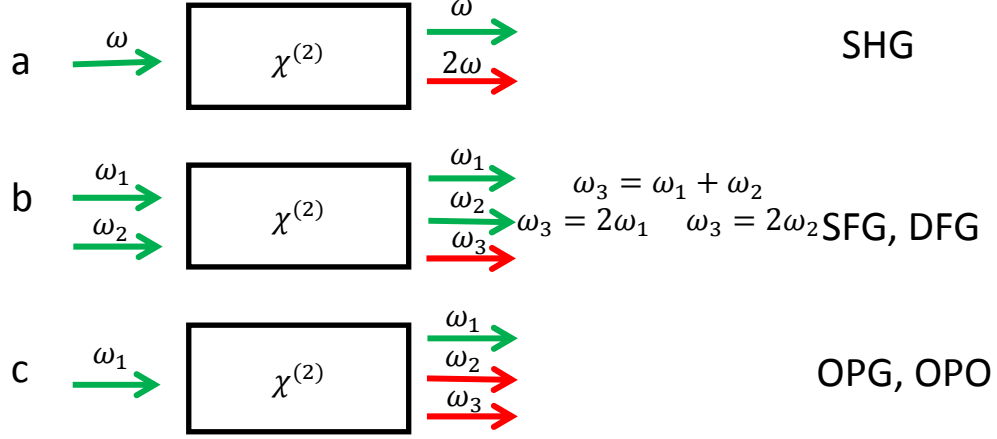

Figure 2.1 Second order nonlinear interaction processes.

Figure (2.1.a) shows the second-harmonic generation process, where two incident photons, each with frequency ω, are combined to give one new photon with frequency 2ω. The induced polarization in the nonlinear medium is then as follows:

$$\widetilde{P}^{(2)} = 2\epsilon_0 \chi^{(2)} EE^* + (\epsilon_0 \chi^{(2)} E^2 e^{-i2\omega t} + c.c.). \qquad (2.5)$$

The first term of Eq.(2.5) represents the zero frequency contribution, known as optical rectification. The second term represents the generated second-harmonic signal with frequency 2ω. Second-harmonic generation is in practice useful to access the spectral range of shorter wavelengths.

Figure (2.1.b) shows the case of sum-frequency generation (SFG) and difference-frequency generation (DFG). In SFG, two incident photons with frequencies ω_1 and ω_2 propagating through the nonlinear medium are combined to creat a photon with higher energy, $\omega_3 = \omega_1 + \omega_2$. In the DFG case, a lower energy photon is created with a frequency of $\omega_3 = \omega_1 - \omega_2$ (observe that here $\omega_1 > \omega_2$).

Figure (2.1.c) shows another possible second order nonlinear interaction called frequency down-conversion or optical parametric generation (OPG). Here, one photon with frequency ω_1 propagating through the nonlinear medium is split into two photons with frequencies ω_2 and ω_3 repectively. If the nonlinear medium is placed in an optical resonator, the configuration is called optical parametric oscillator (OPO) [11].

2.3 Susceptibility coefficient

The nonlinear susceptibility is introduced as a tensor of rank m+1 for $\chi^{(m)}$, but, usually, a nonlinear coefficient, d, is used instead of χ tensor and is defined in the following way:

$$d_{ijk} = \frac{1}{2}\chi_{ijk} \quad . \qquad (2.6)$$

If the condition of permutation symmetry applies, $d_{ijk} = d_{ikj}$, the d-tensor can be expressed as a 3×6-element matrix, and the polarization of the generated photons in Cartesian coordinates is given by the components:

$$\begin{pmatrix} (P_{\omega_3}^{(2)})_x \\ (P_{\omega_3}^{(2)})_y \\ (P_{\omega_3}^{(2)})_z \end{pmatrix} = 2\epsilon_0 K \begin{bmatrix} d_{11} & d_{12} & d_{13} & d_{14} & d_{15} & d_{16} \\ d_{21} & d_{22} & d_{23} & d_{24} & d_{25} & d_{26} \\ d_{31} & d_{32} & d_{33} & d_{34} & d_{35} & d_{36} \end{bmatrix} \begin{pmatrix} (E_{\omega_1})_x(E_{\omega_2})_x \\ (E_{\omega_1})_y(E_{\omega_2})_y \\ (E_{\omega_1})_z(E_{\omega_2})_z \\ (E_{\omega_1})_y(E_{\omega_2})_z + (E_{\omega_1})_z(E_{\omega_2})_y \\ (E_{\omega_1})_x(E_{\omega_2})_z + (E_{\omega_1})_z(E_{\omega_2})_x \\ (E_{\omega_1})_x(E_{\omega_2})_y + (E_{\omega_1})_y(E_{\omega_2})_x \end{pmatrix}, \qquad (2.7)$$

where ω_3 is the frequency of the generated photon due to the annihilation of the two photons with frequencies ω_1 and ω_2. K is the degeneracy factor, given by K=½ , when $\omega_1 = \omega_2$ (SHG case) and K=1 when $\omega_1 \neq \omega_2$[12].

Considering a second-order nonlinear interaction, the susceptibility coefficient $\chi^{(2)}$ only appears in crystals without a center of inversion. In many materials, therefore, $\chi^{(2)}$ vanishes due to their centrosymmetric crystal structure.

2.4 The coupled wave equation

The new frequency components of the electromagnetic field can be expressed by introducing a wave equation. If the nonlinear part is added to the standard wave equation, one can extract the coupled wave equation between the interacting waves by the following expression:

$$\nabla^2 E = \mu_0 \sigma \frac{\partial E}{\partial t} + \mu_0 \epsilon_0 \frac{\partial^2 E}{\partial t^2} + \mu_0 \frac{\partial^2 P}{\partial t^2}, \qquad (2.8)$$

where μ_0 is the vacuum permeability and σ is the conductivity of the crystal.

Assuming a wave propagating in the x-direction. In the second harmonic generation process, it takes the form of plane waves, $E(x, t) = \frac{1}{2}[E(x, \omega)e^{-i(kx-\omega t)}] + c.c$, and with the approximation of a slowly varying electric field, i.e. $\frac{d^2 E}{dx^2} \ll k \frac{dE}{dx}$, the three coupled equations at each frequency, can be derived as following:

$$\frac{\partial E_1}{\partial x} = -\alpha_1 E_1 + \frac{i\omega_1^2}{k_1 c^2} K d_{eff} E_3 E_2^* e^{-i\Delta kx} ,$$

$$\frac{\partial E_2}{\partial x} = -\alpha_2 E_2 + \frac{i\omega_2^2}{k_2 c^2} K d_{eff} E_3 E_1^* e^{-i\Delta kx} , \qquad (2.9)$$

$$\frac{\partial E_3}{\partial x} = -\alpha_3 E_3 + \frac{i\omega_3^2}{k_3 c^2} K d_{eff} E_1 E_2^* e^{-i\Delta kx} .$$

Here, d_{eff} is the effective nonlinear tensor, which depends on the polarization direction of the incident field and can be derived from Eq.(2.7). The term $\alpha_m = \frac{\mu_0 c \sigma}{2}$ is the absorption coefficient and Δk is the total wave vector mismatch of the process and is defined being equal to $\Delta k = k_3 - k_2 - k_1$. For efficient interaction and the highest output intensity, the total phase mismatch should be zero [13].

2.5 Phase-matching

Complete phase-matching is reached when the phase mismatch is equal to zero, $\Delta k = 0$. Considering the SH process, due to the material dispersion, the refractive indices of fundamental and the SH waves differ, $n_{SH} \neq n_F$, so the momentum conservation condition is not fulfilled, i.e. $\Delta k \neq 0$, and the nonlinear frequency conversion is not efficient. Figure (2.2) illustrates the intensity of the second-harmonic signal for different phase matching conditions. For a certain mismatch of Δk, the SHG intensity varies as a function of the crystal length with a period of $L = \frac{2\pi}{\Delta k}$ along the crystal axis. The distance from the crystal edge to the point that the SHG intensity attains its maximum value is called coherence length and is equal to $L_c = \frac{L}{2}$. Over this characteristic distance, a phase difference of π is accumulated between the two interacting waves, i.e., $L_c = \left| \frac{\pi}{\Delta k} \right|$.

After one coherence length, the intensity of the second harmonic field starts to convert back to the fundamental field (no phase matching). In this case, the intensity will oscillate back and forth between the harmonic and the fundamental waves periodically with the coherence length [14].
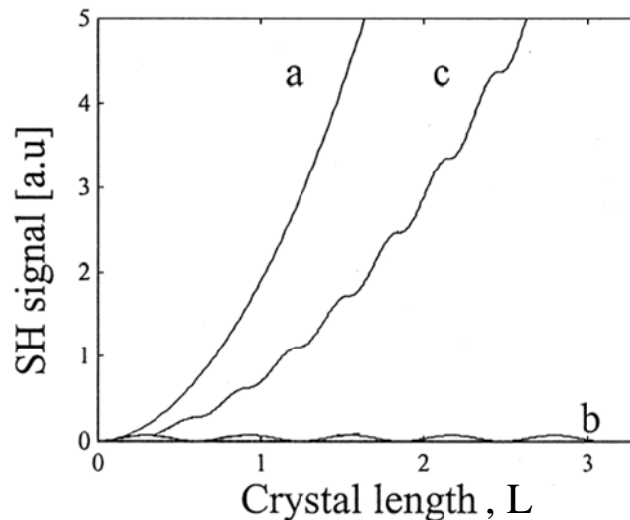

Figure 2.2 Intensity of SHG in different phase matching conditions. a) Perfect phase matching, b) No phase matching and c) Quasi phase matching [14]*.*

Several techniques have been developed to minimize the phase mismatch between the interacting waves. Two different methods will be shortly reviewed with main focus on the concept of quasi-phase matching, which has been employed in this thesis.

2.5.1 Birefringent phase-matching and quasi-phase matching

There are several techniques for compensating the phase mismatch in the crystal. One technique takes advantage of the natural birefringence of the medium itself. The birefringence is defined as the difference between the refractive indices of the ordinary and the extraordinary wave defined on the principal axis of the crystal. In birefringent phase-matching, by choosing a specific "cut" or crystal orientation, the interacting waves experience the same refractive indices. Consequently, they propagate at the same phase velocity and Δk is thus zero. Growth, preparation and alignment of these crystals is straightforward. However, the applicability of simple birefringent phase-matching can be limited by a number of factors. First, since the method relies on the material properties (the dispersion and the birefringence), finding a crystal orientation that satisfies the phase-matching condition is challenging. Second, the nonlinearity depends on the propagation direction in the crystal.

Another phase matching technique, which is based on the compensation of phase velocity differences between the interacting waves, is quasi-phase matching (QPM). In QPM, the sign of the nonlinear susceptibility is modulated in the spatial coordinate to prevent accumulation of phase mismatch. Such a spatial modulation can be obtained in ferroelectric crystals by periodically altering the crystal orientation and in this way the effective nonlinearity changes between $-d_{eff}$ and $+d_{eff}$. The interacting waves still propagate with different phase velocities, but, when the accumulated phase mismatch reaches π, the sign of the driving nonlinear susceptibility is also reversed so that the phase difference is reset to zero. This creates a step-wise growth in the output power along the crystal length as can be seen in Figure 2.2.c. Ideally, the modulation is done after each coherence length, L_c , and is referred to as the first-order QPM. One can also use higher order QPM where the material is modulated with a period of several coherence lengths. Besides a higher efficiency, QPM structures can be made with any period and structure as well as provide phase matching for any nonlinear process inside the transparency window of the material [15].

In a QPM structure, the periodically modulated nonlinear coefficient is used to compensate for the phase mismatch in the crystal. This nonlinear coefficient, d, can be written in the spatial coordinate by a Fourier expansion:

$$d(x) = d_{il} \sum_{m=\infty}^{\infty} G_m \exp(ik_{mQ}x) , \qquad (2.10)$$

where d_{il} is the nonlinear coefficient, k_{mQ} is the mth order grating vector which satisfies the phase-matching condition, and G_m is the Fourier coefficient of the mth harmonic defined as [16]:

$$G_m = \frac{2}{m\pi} \sin(m\pi D). \qquad (2.11)$$

Here, D is the duty cycle, which is determined by the ratio of the reversed domain length and the structure period. From Eq.(2.11) it follows that the most efficient phase-

matching will be for the first order QPM (m = ±1) and with a duty-cycle of 50 % (D = 1/2). Whereas for second-order QPM, efficient phase-matching is gained for a duty-cycle of 25 % (D = 1/4).

2.5.2 Quasi-phase matched second-harmonic generator

The wave vector mismatch for QPM SHG can be written as:

$$\Delta k_Q = k_{SHG} - 2k_F - k_{mQ}, \qquad (2.12)$$

where k_{mQ} , the so called m^{th} harmonic grating vector, is defined as:

$$k_{mQ} = \frac{2\pi m}{\Lambda}. \qquad (2.13)$$

When the SHG and the fundamental waves are quasi-phase matched, i.e., $\Delta k_Q = 0$, the grating structure period can be written as:

$$\Lambda = \frac{2\pi m}{k_{SHG} - 2k_F} = \frac{m\lambda}{2(n_{SHG} - n_F)} \qquad m = 1,2,3,\ldots \ . \qquad (2.14)$$

The length of the grating structure can then be adjusted for maximizing type-I and type-II QPM SHG processes. Type-I and type-II SHG are related to d_{33} and d_{24}, respectively.

2.6 Fabrication methods of QPM structures

In principle, a QPM device can be designed as long as one can change the sign of the nonlinear coefficient in the material. There are several methods, including crystal growth [17], ion exchange [18], and electron beam writing [19], to fabricate QPM devices. However, the most common technique for making QPM structures is electric-field poling. High-quality, periodically inverted ferroelectric domain structures in flux grown $KTiOPO_4$(KTP) crystals were fabricated in the late 90's by Laurell and Karlsson using this technique [20]. A scheme for sample preparation and subsequent electric-field poling is shown in figure 2.3.
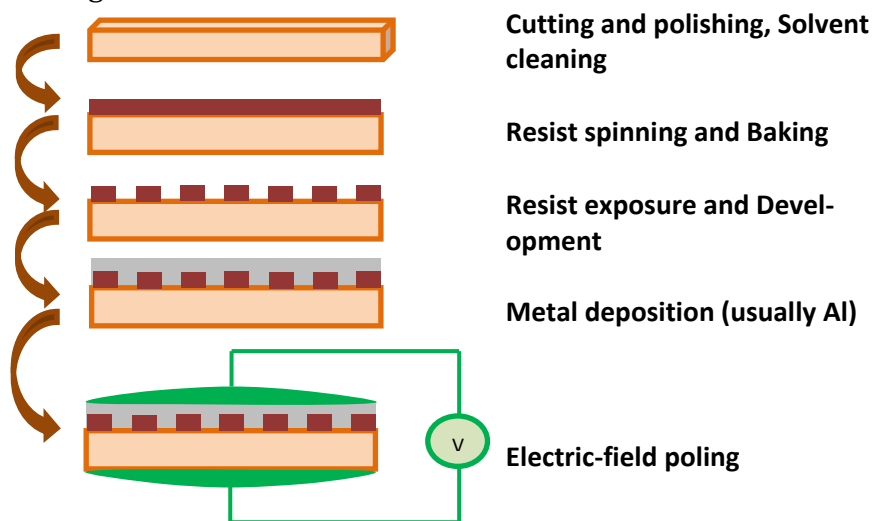

Cutting and polishing, Solvent cleaning

Resist spinning and Baking

Resist exposure and Development

Metal deposition (usually Al)

Electric-field poling

Figure 2.3 Contact electrode poling process.

The ferroelectric crystal is cut into small pieces and the c-face is polished to provide optimum light beam propagation. After cleaning the samples, the photoresist is spin-coated on the polar faces of each crystal. The periodic structure is created by a standard photolithographic process. Finally, metal electrodes are formed by met-al deposition on top of the photoresist. The last step is applying a voltage across the crystal to create the domains of reversed polarization under the metal electrodes.

The QPM devices have a very high efficiency, when the domain structures are uniform through out the whole thickness of the crystal as well as in the direction of the optical beam propagation. Fabrication of periodically-poled crystals can be done only in certain crystal materials. These materials are ferroelectric nonlinear crystals such as KTP, $LiNbO_3$ and $LiTaO_3$.

2.7 1D and 2D quasi-phase matched crystals

For 1D QPM, the incident plane wave is usually propagating in the x-direction and the phase mismatch can be compensated for in a structure with the period Λ, which is equal to a multiple of the fundamental spatial frequency of the structure, $\frac{2\pi}{\Lambda}$. In a 2D crystal, the electromagnetic radiation is propagating in the x-y plane. In this situation, more than one k_{mQ} vector appear which are not in the same direction as the initial plane wave (opposite to 1D QPM). Figure 2.4 shows the possible k_{mQ} in the case of the SHG process for 2D QPM. For a given pump frequency ω, several grating vectors k_{mQ} can compensate for the phase mismatch. By changing the angle of the incident beam one can observe different cases of SH corresponding to these different k_{mQ}'s. Each propagation direction in such a 2D QPM structure can result in several SH peaks with varying intensity [21].
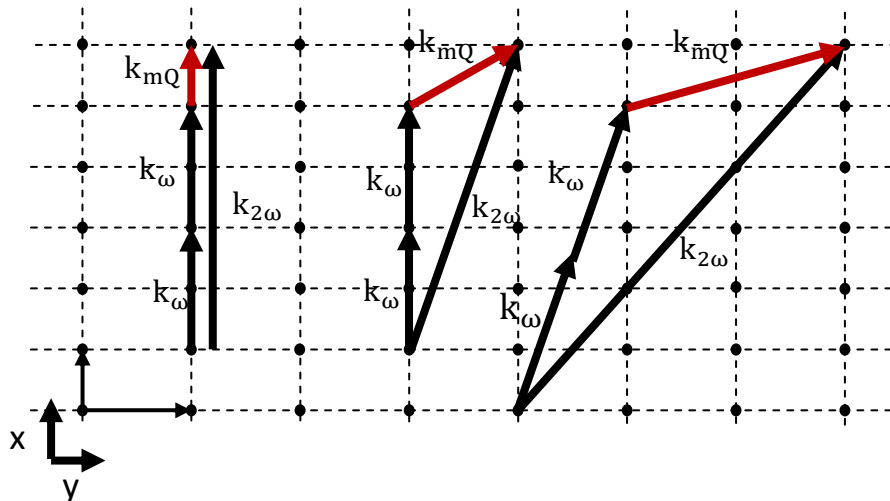

Figure 2.4 Possible k-vectors for compensating phase mismatch in a 2D QPM crystal.

3 KTP and RKTP crystal properties

Implementing of QPM is usually achieved by periodically inverting the spontaneous polarization of a ferroelectric crystal. Two main requirements for such a crystal must be fulfilled in order to be suitable for nonlinear optics: First, a relatively high nonlinearity and second, ferroelectricity. Furthermore, the crystal has to be transparent in the range of the interacting waves. In different environmental conditions and varying light intensities, crystals with stable chemical and mechanical properties are best choices for frequency conversion. Depending on the application and the processing steps, the available size of the crystal is also an important issue. A ferroelectric crystal such as potassium titanyl phosphate (KTP) is a promising candidate because of its high resistance to optical damage, excellent mechanical stability, and high nonlinearity. It has recently also been shown that a slight Rb doping of the KTP crystal (RKTP) facilitates the periodic poling while RKTP has similar properties as KTP with low ionic conductivity [4]. Hence, RKTP is chosen as ferroelectric nonlinear optical material in this work.

3.1 Crystal structure

The crystal structure of KTP is orthorhombic and its lattice constants are: a = 12.819 Å, b = 6.399 Å and c = 10.584 Å. The principal axis, x, y, and, z correspond to the crystallographic directions a, b, and, c of the crystal, where the c-axis is the direction of spontaneous polarization. The crystal structure is shown in Fig.(3.1). The crystal network consists of TiO_6 octahedra chains which are linked by PO_4 tetrahedras. The TiO_6 octahedra consist of short and long Ti−O bonds, which build-up a chiral structure representing a channel along the c-axis. This chiral structure is an important parameter when it comes to domain inversion along the c-axis and will be discussed in Section 3.3. The K^+ ions are located in these channels and are weakly bonded to both the octahedra and the tetrahedra. Appling a voltage as in the electric field poling leads to the movement of these K^+ ions and results in ionic conductivity [22] , [23].

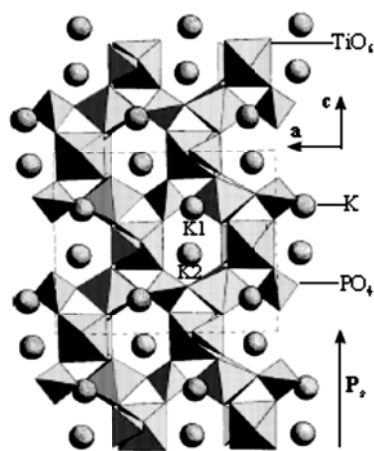*Figure 3.1 The crystal structure of $KTiOPO_4$ [24].*

The nonlinear optical material which is chosen for this project is KTP closest relative, Rb-doped KTP, RKTP. In RKTP crystal, the K^+ ions are substituted by Rb^+ ions. The RKTP crystal has similar properties as KTP with less ionic conductivity.

3.2 Crystal properties

Ferroelectricity

Ferroelectric crystals are materials with spontaneous polarization, which can be switched between two opposing states by applying an electric field. The spontaneous polarization is defined by the composition of negative and positive ions. In equilibrium, the center of positive and negative ions does not coincide. Therefore, each pair of negative and positive ions can be considered as an electric dipole. The sum of these individual dipoles with the same direction constitutes the spontaneous polarization. Any region of a ferroelectric crystal with uniform spontaneous polarization is called a domain. The interface border between each domain inside the crystal is called domain wall. For KTP and RKTP, the domains are oriented along the c- direction forming the 180 ° domain walls between them. The domain walls are parallel to the $\bar{1}00$ crystal plane [25] , [26].

Ionic conductivity

Ionic conductivity plays an important role for the process of domain switching in KTP crystals. The nature of the KTP material allows the diffusion of atoms in the structure. Under certain thermal conditions, the potassium ions (K^+) tend to hop over the vacancies and thereby introducing an ionic conductivity in the c-axis direction. The conductivity along the polar axis can be up to four orders of magnitude larger than the direction perpendicular to the polar axis [25]. High ionic conductivity causes large current to flow through the crystal when a high voltage is applied; this can result in electrical damages of the crystal [27]. In order to decrease the ionic conductivity of the KTP crystal, one can introduce a dopant like Rb. Since Rb^+ has a larger radius than K^+, it is more difficult for the Rb^+ to pass through the conductivity channels in RKTP. The Rb^+ also blocks the lattice for the movement of the majority of the K^+ ions, which otherwise would hop from site to site. This is not possible, since the neighboring spaces are already occupied by Rb^+. The hopping rate of K^+ is then reduced with respect to that of Rb^+ as there are no possibilities for the K^+ ion to pass the Rb^+ ion [28]. The ionic conductivity of RKTP is typically about 2 orders of magnitude lower than that of flux-grown KTP [29].

3.3 Domain switching

Nonlinear crystals such as KTP, which are used for QPM frequency conversion, are grown to have one single domain and are cut along a, b and the c crystallographic axes. In order to alter the polarization, the applied electric field must exceed a certain threshold, called coercive field. The value of the coercive field depends on parameters such as the frequency, the waveform of the applied voltage, the temperature and the shape of the contact electrode.

Ferroelectric domain inversion by contact poling, is based on three steps. First, nucleation of the domain which starts from the edge of each electrode where the field is strongest. Second, the domain will rapidly propagates forward along the polar direction of the crystal and at the same time, the domain will slowly grows sideways [30]. Nucleation is the formation of small antiparallel domains under contact electrodes inside the crystal, which grow and subsequently merge together. These domains can grow both along the ferroelectric axis or by sideways motion. It is estimated that in KTP, the domain-wall growth velocity in the polar direction is, at least, two orders of magnitude larger than in the x-y plane. The velocity along the y-axis is around 30 times larger than that along the x-axis due to the crystal structure of KTP [31]. Domain movement in the sideways directions is not desired in electric field-poling, since it causes deviation from the ideal duty cycle, domain mergings, and will ruin the grating quality.

4 Silicon electrode fabrication

Silicon is a group IV material with unique properties. For example, its conductivity can be controlled over a wide range by introduction of dopants. While this property can be observed in crystalline, poly-crystalline, as well as in amorphous silicon, the single crystalline structure provides high reproducibility and allows devices with high performance to be fabricated. Since Si can be manipulated and fabricated in almost any required shape, it is the first choice material for electrode fabrication.

4.1 Method

There exists a variety of methods for making silicon needles. See, for example, reference [32], where a detailed review of different fabrication techniques for silicon needles masks is given. The technique which would be beneficial for this project needs to be flexible and should be able to make stable and sharp needles with high aspect ratio (height to width ratio). It should also be possible to vary the spacing (or pitch) between the needles.

One of the first methods for fabrication of silicon arrays of needles is based on KOH etching. In this method, the resulting needles have pyramidal shape due to the wet etching following the crystal planes of the silicon substrate. Figure (4.1.a) shows such needles fabricated by a group in USA. This technique is not suitable for the purpose of this thesis because of the following reasons: first of all, the etching process here needs to be stopped at the (111) plane. However, since the etch rate for (411) plane is faster than for the (100), one should have a good control on the etch conditions such as temperature, etchant concentration, and time in order to prevent the needles to become blunt frustums. Furthermore, to achieve a pyramidal shape, the side of the square mask should be aligned along the [110] crystal direction [33]. This mask alignment is critical, thus tedious and time consuming. Beside these problems, making pyramids with smaller periods and still have high aspect ratio structures is constrained by the geometry of the crystal planes, limiting the possibility to vary the pitch.
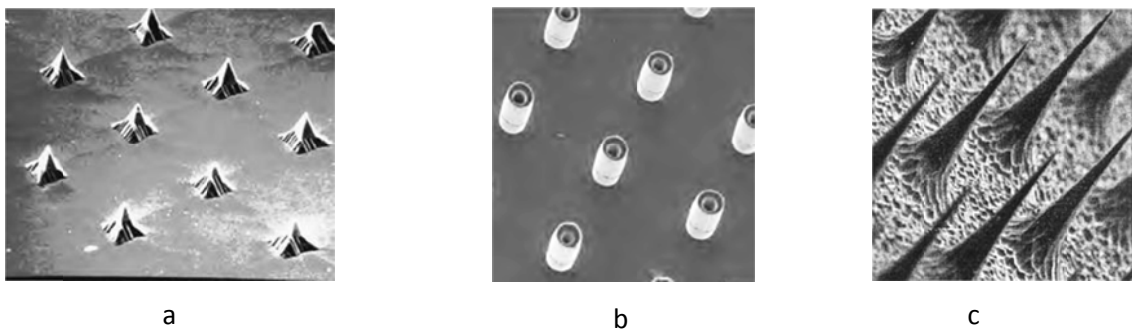

| a | b | c |

Figure 4.1 Various types of silicon needles obtained by different techniques [33] *,* [34] *,* [35]*.*

Another technique is theBosch process. The fabricated electrodes are pillars which have any desirable height . Figure (4.1.b) shows several constructed pillars of 150 μm

height and with a radius of 40 µm made with this technique. The pillars are thick enough to be stable while in contact with the KTP crystals, however, they are not sharp enough and the fabrication process is to some extent, complicated [34].

The third technique for making Si electrodes is a variant of the Bosch process (also termed deep reactive ion etching (DRIE)) where the process parameters are changed during the etching. In this technique, plasma etchants react with the silicon substrate deeply in the vertical direction and slightly laterally, at the same time. The final needles, shown in Fig.(4.1.c), are sharp (1 µm tip radius) and tall (150 µm height). By the use of an optimized ratio of SF_6, O_2 gases, and pressure, the aspect ratio can be adjusted to obtain even taller needles [35]. Although this technique results in the desired sharp needles, a very tall electrode might lead to additional problems due to the high probability of breaking when it comes in contact with the crystals.

Regarding the needles shown in Fig.(4.1.c), one possible solution for reducing the height while the tip radius stays in the micro scale range, is optimizing the etching process. This has been investigated in reference [36] and the resulting modified spikes are shown in Fig.(4.2.a). By using a perfectly isotropic plasma etching (SF_6), the circular mask is under-etched and probes with 20 µm tip radius are fabricated. The diameter of the masks should be twice the desired height of the spikes. Therefore, for fabricating spikes of 200 µm height, the distance between the spikes needs to be 400 µm.
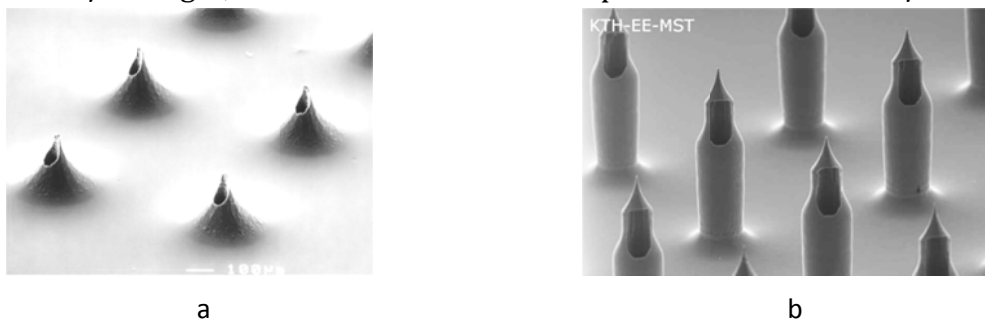
a   b

Figure 4.2 a) silicon spikes and b) long, sharp needles [36] *,* [37]*.*

Roxhed *et al.* have modified the silicon micro probe fabrication process [37]. Their approach is based on alternating between isotropic SF_6 plasma etching and anisotropic deep reactive ion etching through the Bosch process. The isotropic etching determines the curvature of the needle tip and the anisotropic etching determines the height of the needles. The fabrication process is followed by *oxide sharpening* which results in needles with a tip radius below 100 nm, see Fig.(4.2.b).

The method used in this work to fabricate Si micro-needle array-electrode for electric-field poling, is the modified isotropic SF_6 plasma etching. Since different periods between the needles are wanted, the fabrication process starts with 4-inch silicon wafers that can include 86 chips with 4×8 mm^2 dimension. Furthermore, batch processing is used to fabricate several wafers simultaneously. The lithography mask is designed to obtain needles with a height of 1 - 2 µm.

4.2 Photolithographic mask design

The design of the photolithographic mask for the silicon array of neeles fabrication contains seven different periods in square and in hexagonal arrangement. The distance between the needles in the different arrays includes: 3.2 μm, 5 μm, 6.4 μm, 8 μm, 9 μm, 15 μm and 20 μm. For having sharp needles of 1-2 μm height, a circular mask of roughly 4 μm diameter should be designed for each needle as it is shown in Fig.(4.3). However, this 4 μm diameter value cannot apply for the 3.2 μm period due to the distance restriction. For the 3.2 μm period, the circular mask diameter is taken to be 2.2 μm. Thus the height of the needles for this period will be smaller than for the other periods.
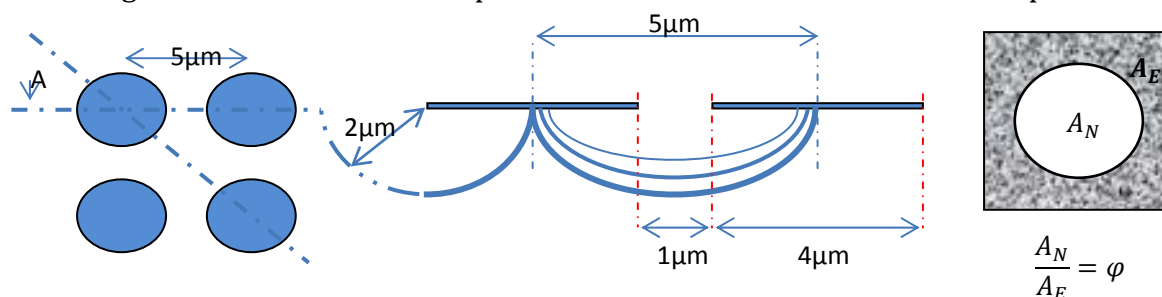
Figure 4.3 Schematic of mask, opening area and ratio of exposed and non-exposed area for a 5 μm period grating.

The period diversity for different electrode array results in specific density of circular masks on each array. Furthermore, considering the same diameter of the circular mask for the period of more than 5 μm, the opening area (etch area) will be different for each array. The opening area increases by increasing the period. These two reasons, besides the fact that the etch rates are not the same for all parts of the wafer (due to gas and plasma distributions in the chamber), lead to the predicted non-identical needle shapes on the arrays with different periods. One way to control these parameters is to calculate the 'exposed area' (etching area) and the 'non-exposed area' and arranging different electrode arrays with regard to the high and the low etch rate parts of the wafer. Figure (4.3) shows a schematic of the mask, the opening area and the estimated etching shape for a 5 μm period. The parameter φ represents the ratio between the exposed and the non-exposed area for this period.

After calculating the value for φ for all the specific periods, arrays with higher φ value were located close to the perimeter of the wafer, where the etch rate is higher, whereas arrays with lower φ value were located in the center part where the etch is slower. Table (4.1) summarizes the different parameters of each array regarding the opening areas, mask diameters and the corresponding φ value.

Period (µm)	Type	Mask diameter (µm)	A_N: Non-exposed area	A_E: Exposed area	$\varphi = A_N/A_E$
3.2	Hexagonal	2.2	3.73	5.02	0.74
	Square	2.2	3.73	6.38	0.58
5	Hexagonal	4	12.56	9.09	1.38
	Square	4	12.56	12.44	1.01
6.4	Hexagonal	4	12.56	22.86	0.55
	Square	4	12.56	28.44	0.44
8	Hexagonal	4	12.56	42.64	0.29
	Square	4	12.56	51.44	0.24
9	Hexagonal	4	12.56	59.14	0.21
	Square	4	12.56	70.25	0.18
15	Hexagonal	4	12.56	182.2	0.07
	Square	4	12.56	212.44	0.06
20	Hexagonal	4	12.56	333.85	0.04
	Square	4	12.56	387.44	0.03

Table 4.1 Mask diameter, exposed and non-exposed areas for different gratings on the wafer.

Although the arrangement of the arrays was done to get the same result in all cases, a large difference in the φ value lead to anticipated different needle shapes. Comment: The less exposed area open to the etch gases there is on the wafer, the more uniform etch results will yield (due to less consumption of etch-gas molecules and thus a more homogenous etch plasma with less excausted volumes). In reality, very low φ:s are unpractical, as you get very few etched features on your wafer.
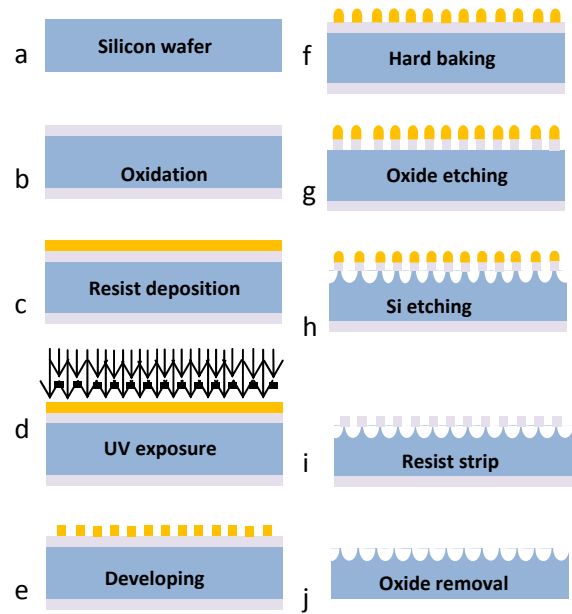

Figure 4.4 Schematic of the fabrication process.

4.3 Fabrication process

The process started with five one-sided, 500 µm thick, p-doped wafers. The dopant element was boron, the wafer orientation was (100) and the resistivity was 0.005 - 0.02 Ωcm. These characteristics made the wafer suitable for the contact electrode poling. A schematic of the fabrication process is illustrated in Fig.(4.4).

4.3.1 RCA cleaning

The first phase of the process is wafer cleaning (Fig.(4.4.a)) to eliminate any contamination, and also to prepare the wafer for a better adhesion of the photoresist. The standard cleaning procedure contains four steps:

1. Removing organic contaminants by placing the wafers into a solution of H_2SO_4+ H_2O_2 at 80-130 °C for 5 minutes, a.k.a. Piranha dip or 7-Up cleaning.

2. Washing in deionized (DI) water N_2 bubbler for 5 minutes.

3. Removing the thin native oxide layer ($\sim$10 Å) by putting the wafers into a solution of HF (50 %) + H_2O at 25 °C for 100 seconds.

4. Washing again in DI water and bubbler for 3 more minutes, followed by drying in hot N_2

4.3.2 Wet oxidation

After cleaning the wafers, they were transferred to the 'wet' (O_2 and H_2) oxide furnace (Fig.(4.4.b)). The oxide growth rate at 1050 °C is approximately 5.3 nm/min. Therefore, a 1 µm thick oxide layer, requires a three hours run. The oxide layer will later act a hard mask for the silicon needle fabrication, being resistant to the SF_6 etch plasma.

4.3.3 Resist coating

The resist coating is illustrated in Fig.(4.4.c). It includes four steps that are performed semi-automatically:

To prevent peeling of the resist, the wafers were coated with an adhesion layer consisting of hexamethyldisilazane (HMDS) at 130 °C. The surface oxide layer on the wafer forms long-range hydrogen bonds with water absorbed from the air. When resist is spun onto such a surface, it adheres to the water vapor rather than to the wafer surface, and this results in poor adhesion. Before applying the HMDS, the temperature of the chamber was increased to 130 °C in order to dehydrate the surface. Then HMDS gas was spun onto the dehydrated surface, providing a more efficient adhesion of the photoresist. The wafers then had to be cooled down to 22°C in 20 seconds to prevent a reduction of the resist viscosity. The photoresist (SPR 700 1.2) was spin coated with 5000 rpm on the wafers resulting in the final resist layer being 1.2 µm thick. To evaporate the solvent and prepare it for exposure, the wafers were soft baked on a hot plate at 90 °C for 60 seconds. Exposing a wafer without cooling it down results in a thermal expansion effect of the photoresist.

4.3.4 UV exposure

The UV exposure step is one of the challenging parts of the fabrication process due to the fact that it requires high resolution to achieve micron-scale structures. Critical pa-

rameters are the wavelength of the UV light and the exposure time. The wavelength of the mask aligner was set to 405 nm with an intensity of 18.4 MWcm^{-2}. The exposure time can be calculated by knowing the UV lamp's intensity and the thickness of the photoresist, however, it needed modification for getting good lithographic results.

Reproduction of the photolithographic mask structure on to the photoresist was done by 'proximity exposure' which retains a gap between the mask and the wafer to prevent stiction or damage (Fig.(4.4.d)). Since the wavelength of the UV light is comparable with the mask features, the gap may cause some diffraction effects and may degrade the resolution of the pattern. Therefore, the gap also needed to be modified. The UV exposure step was started with four different parameters to optimize the process. The exposure time and the lamp intensity were kept at the same level but the exposure mode and the gap between wafer and mask were changed. The detailed parameters are listed in Table (4.2).

	Mode	Exposure time	Gap	Lamp intensity
Wafer 2	Soft contact	5 s	50 µm	18.4 MW/cm^2
Wafer 3	Soft contact	5 s	40 µm	18.4 MW/cm^2
Wafer 4	Vacuum contact	5 s	50 µm	18.4 MW/cm^2
Wafer 5	Soft contact	5 s	30 µm	18.4 MW/cm^2

Table 4.2 Exposure parameters for 4 different wafers in batch process. Wafer 1 is not listed since it is used as dummy.

4.3.5 Developing

Developing the exposed photoresist began with a 60 seconds soft-bake step at 110 ℃ in vacuum followed by a 15 seconds cooling down to 22 ℃. The soft bake rearranges the exposed and non-exposed molecules of the photoresist, averages the standing wave intensity and prevents over-exposure and/or under-exposure. Moreover, it smoothens the photoresist side walls and increases the resolution [38]. The baking was followed by developing the photoresist in a CD26 developer. The CD26 developer is a combination of <95 % water and 3% tetramethyl ammonium hydroxide. This developer reacts with the exposed photoresist and the hydroxide carboxyl groups of the photoresist are dissolved in it. The final profile is depicted in Fig.(4.4.e).

4.3.6 Hard bake

Before continuing the process with dry etching, the wafers needed to be hard baked. Hard baking decreases the etch rate of the photoresist and prevents the total consumption of the resist during the etch process. Furthermore, during the hard bake, all the solvent in the photoresist is evaporated, which improves adhesion of the photoresist.

The hard-bake time needed to be adjusted due to the type of photoresist employed and its thickness. An under-baked photoresist has low adhesion, is not polymerized properly and displays high etch rate. On the other hand, over-baking of the sample re-

sults in reflowing of the photoresist in the openings and will thereby degrade the resolution.

In this experiment, our samples were hard baked for 45 minutes at 110 ℃. Fig.(4.4.f) illustrates the sample after the hard baking stage.

4.3.7 Silicon oxide etching

In this step, the hard mask (SiO_2 layer) was patterned through the photoresists soft mask by etching. The process was performed in a dry-etching machine with a combination of gases: N_2, Ar, O_2, CF_4 and CHF_3. The estimated oxide etch rate in this machine was 60 nm/min. Considering the the oxide thickness should be 950 nm, the samples were processed for 16 minutes. Fig.(4.4.g) shows the scheme of the sample after removing the oxide layer.

4.3.8 Silicon etch

The silicon was etched isotropically through the openings of the oxide (hard mask) to form the needles by using SF_6 in the reactive ion etching machine. To set the running time of the process, the etch rate needed to be estimated. The rate depends on several adjustable parameters: pressure, initial pump-out time, speed flow of the plasma and plasma power type can be varied. A detailed description of these parameters can be found in [37]. However, based on this reference, the time estimation for needles of 1-2 µm height is 65 seconds. The final needle arrays are supposed to look like those shown in the scheme of Fig.(4.4.h).

4.3.9 Masks strip

After forming the needles, the next step was removing the masks and exposing the silicon needles. The removal of the photoresist was done by applying an oxygen plasma for 15 minutes with 500 sccm at 1000 W (Fig.(4.4.i)). The oxide mask was removed from the wafer by dipping it in hydrofluoric acid (50 %) . Hydrofluoric acid is a good option in this case due to its selective etching of the silicon oxide. 2 minutes was found to be sufficient etch time. Rinsing wasin DI water for 30 seconds. The most reliable way to ascertain the point when the oxide is completely removed from the wafer is testing it with DI water. Since silicon oxide has a hydrophilic surface, if after this step, if a film of DI water is still observed on the whole wafer, the oxide has not been properly removed. This process was continued until the surface showed a hydrophobic behavior, which means that the oxide layer was removed [38]. Figure (4.4.j) shows the final needles shape on the silicon wafer after removing the masks.

4.4 Modifications

High-density patterns (5 µm periodicity) and low-density patterns (20 µm periodicity) in the same photolithographic mask introduced difficulties in the photolithography and the silicon etching steps. Different etch rates due to the different openings may result in

varying height of the needles. However, it can be modified by arranging different arrays on the same mask as it was explained in Section 4.2. Considering the lithographic problems, the diffraction effect due to the small gap between the mask and the wafer, photoresist spreading after the hard bake and a non-optimal exposure time will lead to a poor lithographic quality in many of our patterns. Moreover, a small period between each single circular masks, resulted in a higher risk of over-exposure due to contamination between exposed and non-exposed photoresist and decreased quality of the lithography. Using vacuum contact exposure mode and thus decreasing the gap size and the exposure time resulted in better resolution for different feature sizes.

Regarding the silicon dioxide and the photoresist mask, which are used for the patterning and silicon etching, their layer thickness is a challenging issue in the fabrication process. For having well-controlled etching of silicon, a relatively thick silicon oxide layer is needed. This, consequently, requires longer oxide etching time. On the other hand, a longer silicon oxide etching directly results in a higher photoresist consumption. Thus, a thick layer of photoresist is needed which possibly results in a poor pattern quality. However, a thinner photoresist layer also requires a thin oxide layer. This leads to not well-controlled silicon etching and, again, low resolution in pattern quality. Therefore, the thicknesses of these two layers needed to be optimized. The optimization which was used in this thesis was a thinner oxide layer and a slightly thicker photoresist layer with regards to their initial values. Hard baking time was decreased in order to prevent reflow of the photoresist in the openings. The initial and modified values of the different parameters are listed in Table (4.3).

	Oxide thickness	Photoresist thickness	Exposure time	Proximity mode	Proximity gap	Hard bake time
Initial	950 nm	1.2 μm	5 s	Soft contact	30-50 μm	45 min
Modified	470 nm	1.4 μm	4 s	Vacuum contact	10 μm	30 min

Table 4.3 Initial and final parameters for needles fabrication.

4.5 Final fabricated Si electrodes

The fabrication process of the silicon micro needles has been optimized in every fabrication step in order to construct needles with the desired period and dimensions. However, due to the reasons mentioned in Section 4.4, the resulting needles have different shapes. Figures (4.5) - (4.8) illustrate 5 μm period patterns in different steps of fabrication.
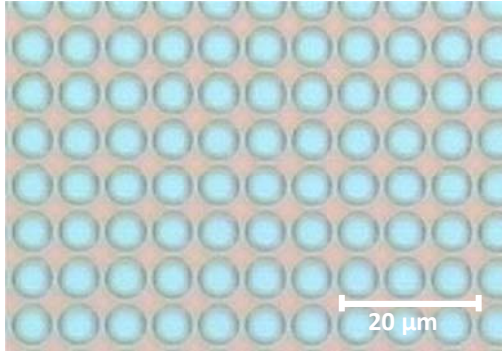
Figure 4.5 Optical microscope image of 5 μm period pattern after lithography.

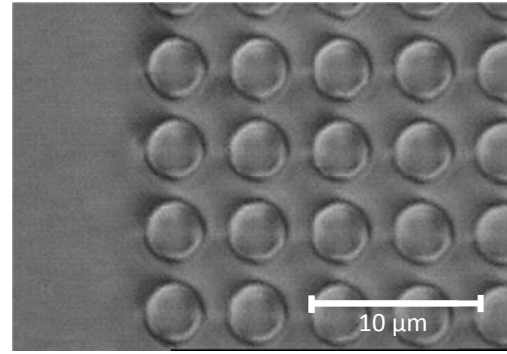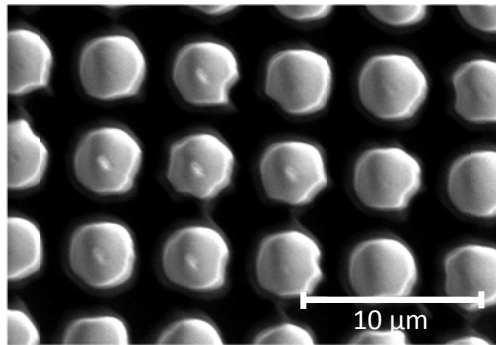*Figure 4.6 Optical microscope image of 5 μm period pattern after oxide etching.*

Figure 4.7 SEM image of 5 μm period pattern after isotropic Si etch.

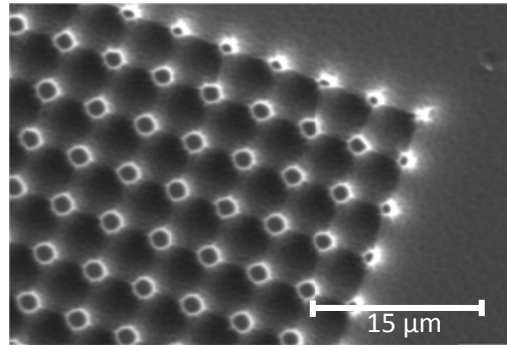*Figure 4.8 SEM image of 5 μm period after mask removal, formation of plateaus.*

For the 3.2 μm period patterns, when the Si etch process was being stopped, the circular masks collapsed on the surface due to over-etching (Fig.(4.9) - (4.12)). The first reason for the collapsing for this period is the fact that the circular mask diameter was 2.2 μm for this pattern which is smaller than for the other periods (4 μm diameter for the rest). The second reason is having a variable circular mask density on one wafer. The same etch duration for the 3.2 μm, 5 μm and the 20 μm cases resulted in over-etching, plateau-shaped electrodes, and very sharp spikes, respectively.

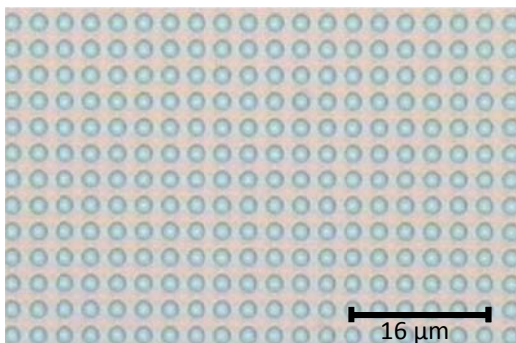*Figure 4.9 Optical microscope image of 3.2 μm period pattern after lithography.*

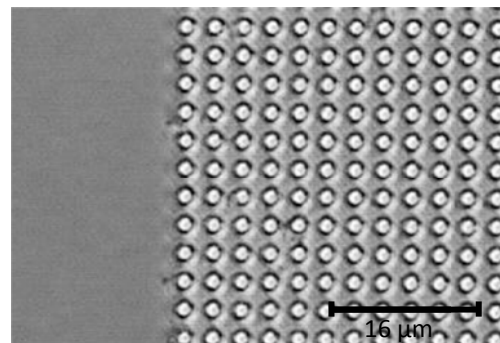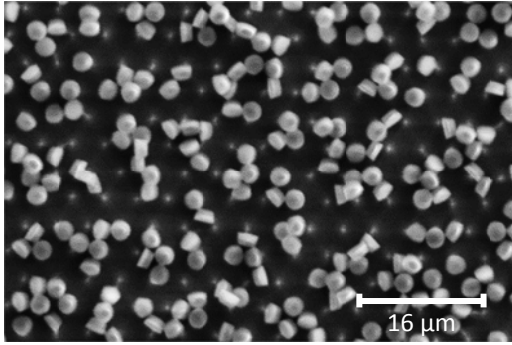*Figure 4.10 Optical microscope image of 3.2 μm period pattern after oxide etching.*

21

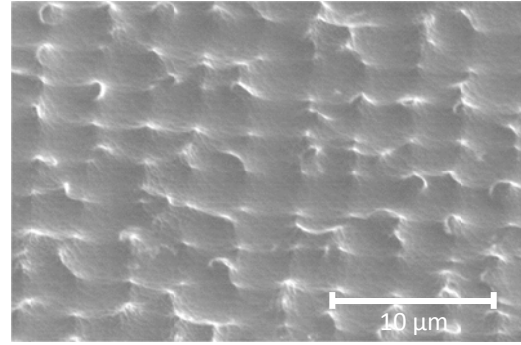*Figure 4.11 SEM image of 3.2 µm period pattern after isotropic Si etch, masks drop.*

Figure 4.12 SEM image of 3.2 µm period pattern after mask removal, over etched pattern.

Figure (4.12) shows the patterns after removing the collapsed circular masks from the surface with 3.2µm periods. Since the circular masks collapsed during the isotropic etching process, their trace on the surface damaged the whole pattern.

Unlike the patterns with 5 µm periods and 3.2 µm periods, which are under-etched and over-etched, respectively, the patterns with 20 µm periods are isotropically etched and the undercut is exactly equal to the circular mask diameter (4 µm). As a consequence, in these patterns, the spikes are very sharp with a tip diameter less than 1 µm. Figures (4.13) - (4.16) show the pattern images after the lithography, silicon oxide etching, ICP etching of the Si and the masks removal steps for the 20 µm period pattern, respectively.
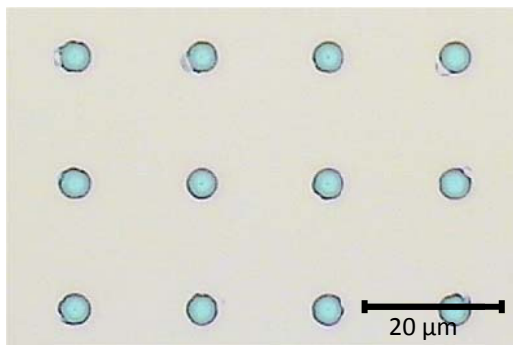

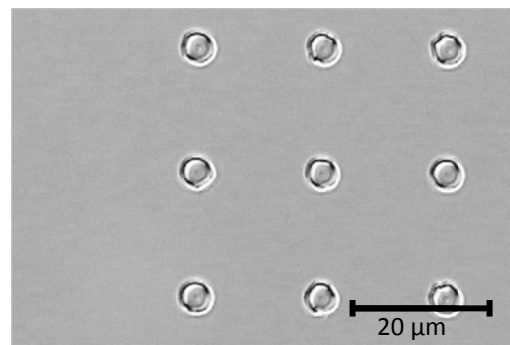*Figure 4.13 Optical microscope image of 20 µm period pattern after lithography.*

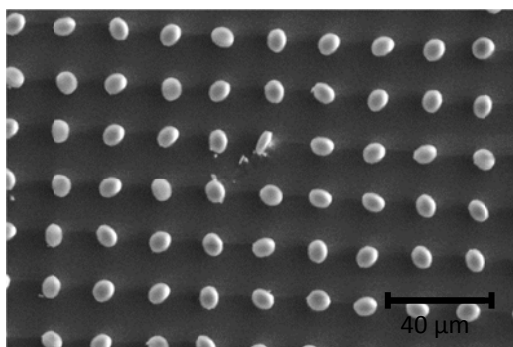*Figure 4.14 Optical microscope image of 20 µm period pattern after oxide etching.*

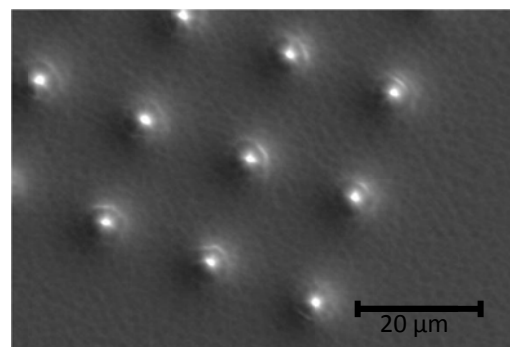*Figure 4.15 SEM image of 20 µm period pattern after isotropic Si etch.*

Figure 4.16 SEM image of 20 µm period pattern after mask removal, needles are formed.

Despite overetching as well as not-enough etching, the fabricated spikes and plateaus could be used for intended use; periodic poling. Their height and top diameter are important. For the 20 μm period pattern, the spikes have a height of 1.73 μm, with a slight variations over whole surface of the silicon electrode. The tip diameter of the spikes is approximately 50 nm, which is satisfactory for the purpose of this thesis, as shown in Fig.(4.17) – (4.18). Regarding the 5 μm period pattern, the plateaus have a height of 2.8 μm and a top diameter < 2 μm, as shown in Fig.(4.19) – (4.20).

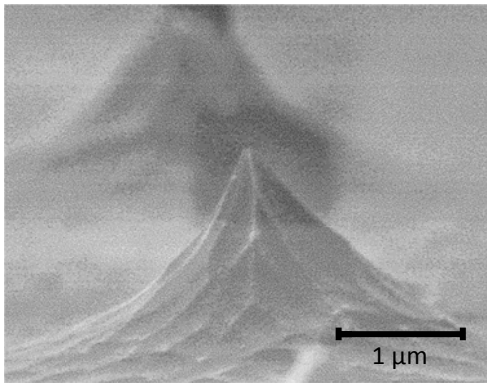*Figure 4.17 SEM image of a needle in 20 μm period pattern with height of 1.73 and tip diameter of 50 nm.*

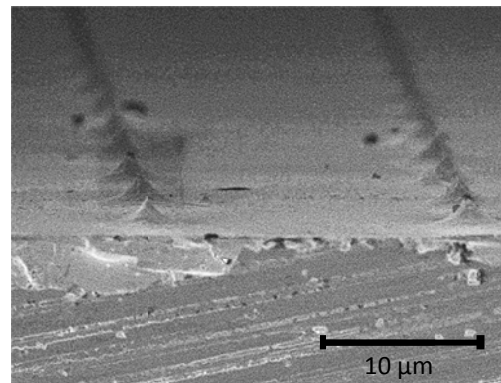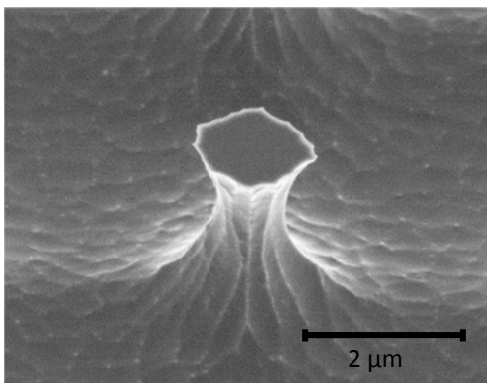*Figure 4.18 SEM image of 20 μm period pattern.*

Figure 4.19 SEM image of a needle in 5 μm period pattern with height of 2.8 and top diameter of approximately 2 μm

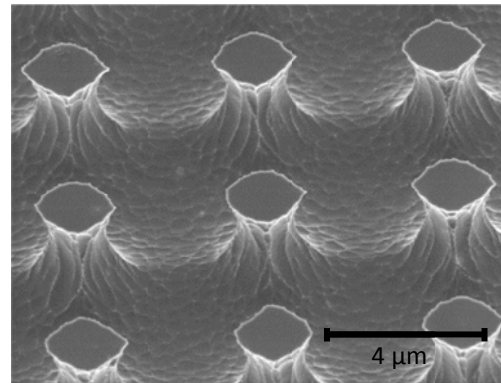*Figure 4.20 SEM image of 5 μm period pattern.*

5 Fabrication of periodically poled RKTP by silicon stamp

Considering the fabrication of QPM crystals with electric-field poling, the most common defects in the fabrication are missing/merged domains and domain broadening. Fabricating sub-micron structures becomes more challenging since the fringing-field effect is more severe. In this case, the usual technique for patterning of the metal electrode on the sample surface is photolithography process (see Section 2.6). The photolithography process involves several steps which must be performed on the surface of each individual sample. This process is time consuming and can lead to slightly different patterns on each sample. Furthermore, by having the same thickness of photoresist, in sub-micron domain fabrication, the aspect ratio is increased and the quality of photolithography is decreased. Therefore, the lithography process needs to be modified in order to achieve high quality in the fabricated domains with less defects.

In this work we investigate a new technique of electric field poling using a boron-doped silicon array of needles as an electrode. Unlike the previous techniques, here the whole array of electrodes is manufactured independently from the crystal on a silicon wafer. Silicon is a flexible and highly developed material, therefore, transferring lithography steps from the crystal surface to a Si electrode can be helpful in order to overcome the photolithographic problems of the conventional technique. As illustrated in Fig.(5.1), the fabricated silicon array of needles is mounted on the crystal and the polarization is altered by applying a voltage across the crystal and the whole electrode structure.
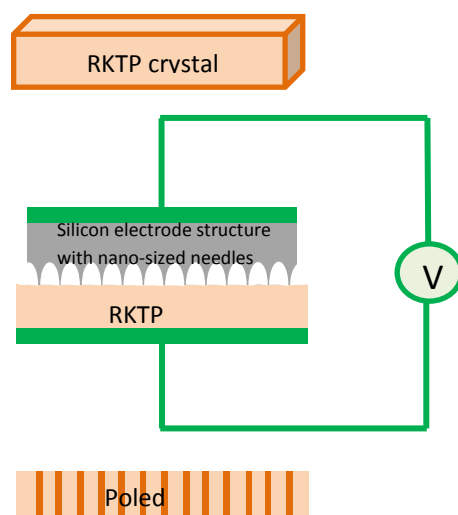
Figure 5.1 Schematic of poling technique with silicon electrodes.

In order to study the electric-field poling using the Si electrode, different electrode gratings with different periods ranging from 3.2 μm to 20 μm were fabricated. The top dimension of each electrode on the surface vary between 50 nm and 1.9 μm. With the help of the silicon array of electrodes, the periodic poling can be done using fewer steps and only one silicon electrode structure can be used for poling of several samples.

In this chapter, periodic poling with this technique is discussed. Furthermore, the quality of the created domain structures is studied and the optical performance of periodically-poled crystals is evaluated.

5.1 Sample preparation

The material used in this work is Rb-doped potassium titanyl phosphate (RKTP). The RKTP wafer was cut into samples of dimensions $10 \times 5 \times 1$ mm along the a, b and c crystallographic axes, respectively. Since the conductivity mainly varies along the y-direction in each wafer, each column in the x-axis was expected to have more or less the same conductivity [20]. Therefore, during the cleaning procedure, the samples should be kept in the same order as in the initial wafer box to make further analysis simpler.

5.2 Poling setup

The poling setup included a holder and an electric circuit which was used for applying the high voltage. The sample holder consisted of two liquid electrode cells which are shown in Fig.(5.2), and were used to fix the electrode structure and the crystal to each other and to keep them in contact. The silicon electrode was centered on top of the crystal manually. The crystal and the silicon electrode were connected to the circuit by a saturated KCl solution which gives a more uniform connection over the whole surface of the crystal and the silicon electrode.
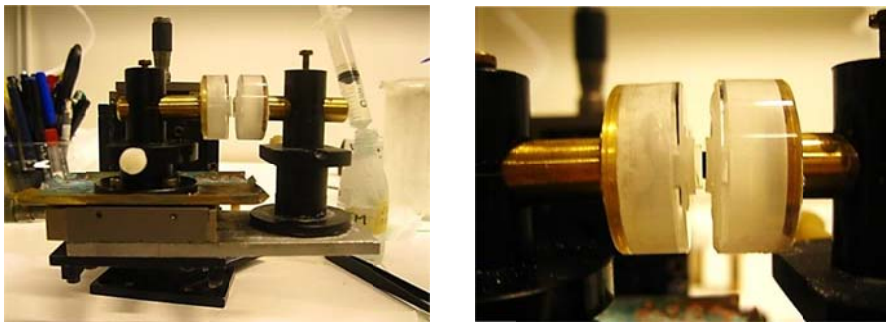

Figure 5.2 Poling cell.

5.3 Fabrication of PPRKTP

Several parameters can be adjusted during the poling process in order to achieve the best results. The pressure between the crystal and the electrode, the electric-field pulse duration, the pulse shape and the magnitude of the applied electric field are such parameters. In the frame of this work, all parameters were set at constant values except for the applied voltage. The pressure between the crystal and mask could not be ideally controlled (due to the manual aligning and mounting). Since the poling process is a rapid one, the electrical pulses were chosen to be triangular with a duration of 5 milliseconds. Short electric-field pulses decrease the domain spreading beyond the electrodes [4]. The silicon electrode structure was connected to the c^+ polar face of the crystal and the nucleation started from this face. The polarization inversion was executed for 24

RKTP samples. Two different silicon masks, with a periodicity of Λ = 5 μm and Λ = 20 μm, were used for the periodic poling.

5.4 Poling monitoring

In low-conductivity ferroelectrics such as LiNbO$_3$, the domain inversion can be controlled by monitoring the current flowing in the poling circuit [2]. For high-conductivity ferroelectrics, such as KTP, the applied field leads to a strong ionic current passing through the sample. Therefore, monitoring the poling process by the current flow is inaccurate. In order to control the poling, and to be able to reproduce the results, the poling process was instead monitored by the electro-optic effect and in-situ SHG.

A schematic of the experimental setup is shown in Fig.(5.3). The HeNe laser beam was linearly polarized 45° to the z- and y-axis of the crystal by the polarizer. The beam went parallel to the x-axis of the crystal and the intensity of the beam was measured by an analyzer rotated by 90° with respect to the first polarizer. When the domains propagate down through the crystal, the output intensity from the HeNe laser will be modulated in the crystal [39]. This effect can be observed with a photodetector and an oscilloscope.
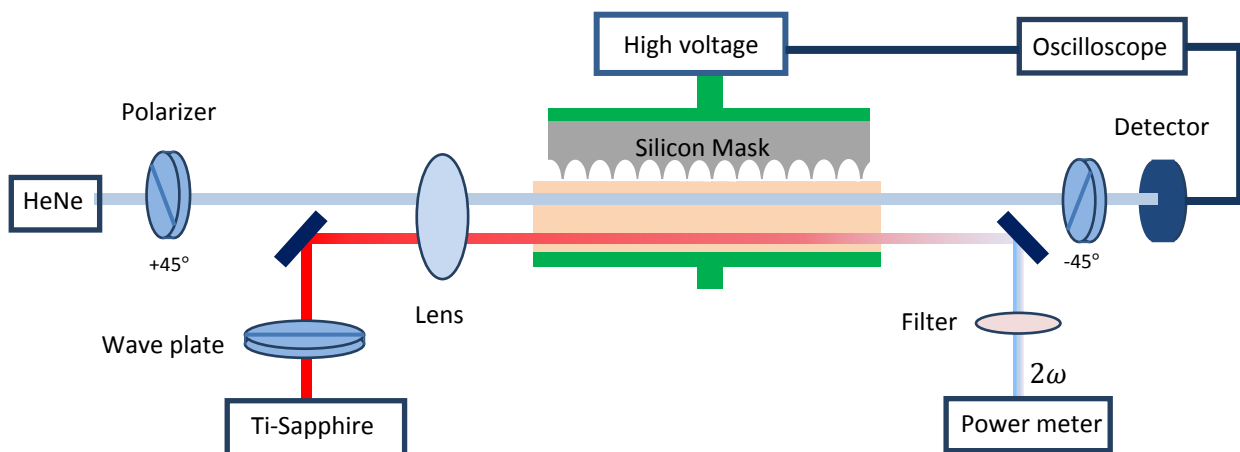

Figure 5.3 Poling monitoring setup.

The electro-optic monitoring method gives information as to whether the polarization is reversed or not. Hence, only a qualitative indication of the poling result can be obtained by this technique.

In order to obtain more detailed information on the homogeneity of the fabricated domains, the in-situ SHG technique was applied [29]. A Ti:sapphire laser was loosely focused on the crystal aperture and tuned to the phase-matching wavelength. The SHG signal was measured by a power meter. The laser beam was scanned in the horizontal and the vertical directions to check the quality of the domains by observing the SHG in different positions across the crystal aperture.

As a CW Ti:sapphire laser (Spectra Physics Model 3900S, pumped by a 10 W Milennia X_s) has emission lines between 700 nm and 950 nm, the QPM grating period of 5 μm can be evaluated by using the 1st order SHG, i.e., $\lambda_F = 894$ nm. For the periods of $\Lambda = 20$ μm the 5th order SHG has to be used with a fundamental wavelength of $\lambda_F = 842$ nm (according to Equation 2.14).

6 Characterization of domain structures

6.1 Selective etching

The domain structure after poling was revealed by a selective etching of the samples. The sample was placed in a solution of KNO_3 and KOH (2:1 mole ratio) in 20 ml water at 80 °C for a time typically ranging between 5 - 15 min. The etchant attacks the c^- surface of the RKTP crystal while the c^+ surface is left essentially untouched, thus revealing the domain structure [40].

6.1.1 Domain evaluation for the 20 µm period grating

It was observed that the domain shape and dimension in the case of the Λ = 20 µm samples are not homogeneous. Some parts of the poled samples exhibit domains with a 2D structure on the c^+ polar face. However, corresponding domains on the c^- polar face of the crystal features a 1D structure. The reason for this kind of domain merging can be explained by anisotropic domain growth in the KTP crystal, as discussed in Section 3.3. Nevertheless, a 2D domain structure has been successfully fabricated on both polar faces in some of the RKTP samples.

Both of the polar faces contain 1D and 2D domain structures due to the non-uniform contact (Fig.(6.1)). This non-uniformity is caused on one hand by slight variations in the height of the spikes leading to an inhomogeneous electrode contact. On the other hand, the poling cell is not optimized for electric-field poling with this new technique. The crystal and the silicon electrode are pressed together in the poling cell which results in uniform contact in some areas of the sample and non-uniform contact in other parts.
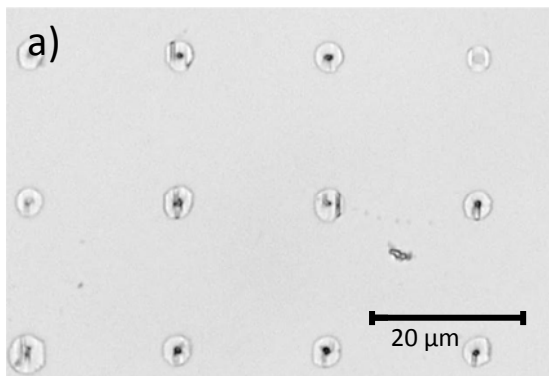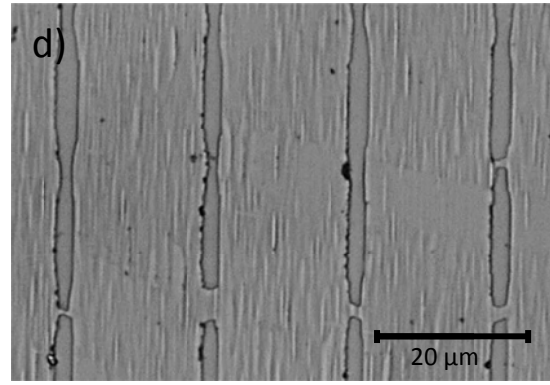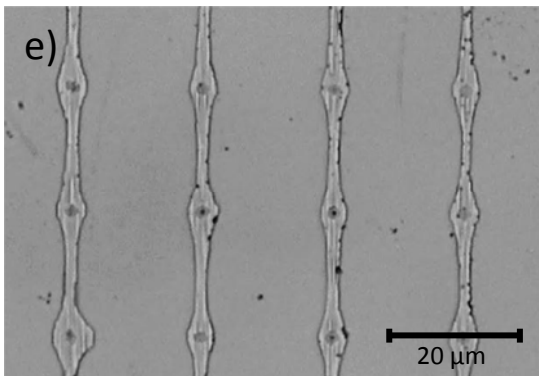

a: c^+ Domain dimension 3.7 × 3.7 µm.
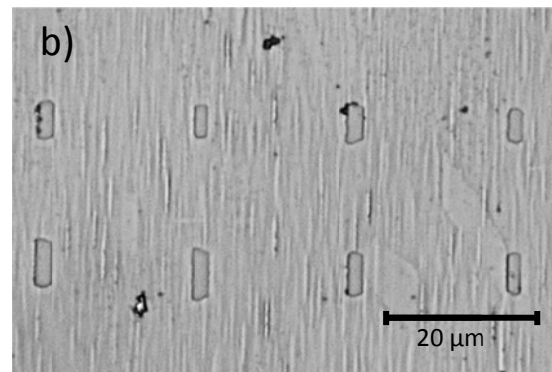
b: c^- Domain dimension 1.5 × 3.7 µm.
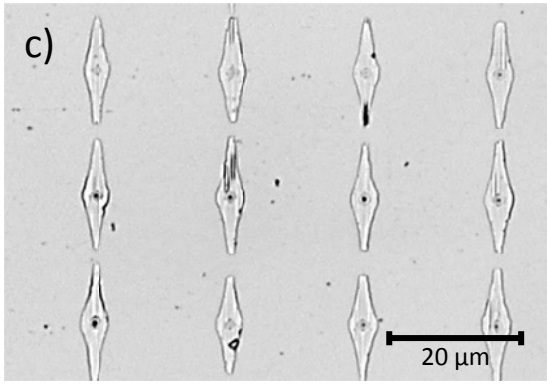
c: c^+ Domain dimension 3.9 × 16 µm.

d: c^- Domain width 3 µm.

e: c^+ Domain dimension 5 µm at the place of needles, 1.6 µm in between.
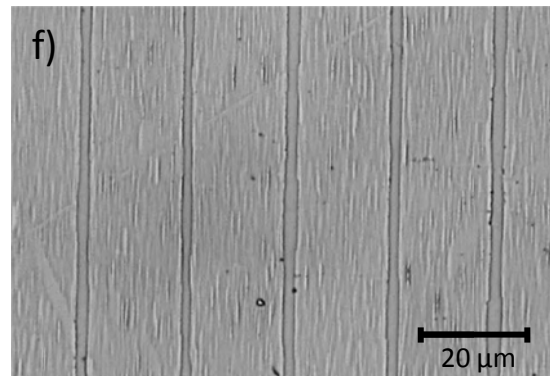
f: c^- Domain width 2 µm.

Figure 6.1 Domain structures of a poled RKTP sample with 20 µm grating period of Si stamp. Applied electric field is 5.8 kV/mm with the triangular pulse of 3 ms duration.

For the 20 µm grating electrode, the density of spikes over the electrode surface is low and spike tips are very sharp. Therefore, the pressure on each single spike is high resulting in many broken spikes and, thus, a net inhomogeneous contact. The initial height of spikes for this period was 1.73 µm with a tip diameter of 50 nm. However, after pressing the crystal and the Si electrode together in the poling cell, the height is reduced to 1.6 µm and the tip diameter is correspondingly reduced to 500 nm, see Fig.(6.2.a) and Fig.(6.2.b).

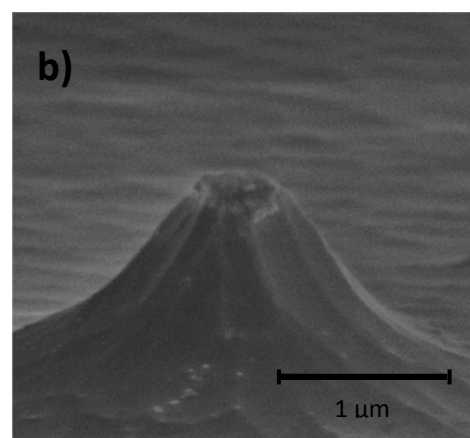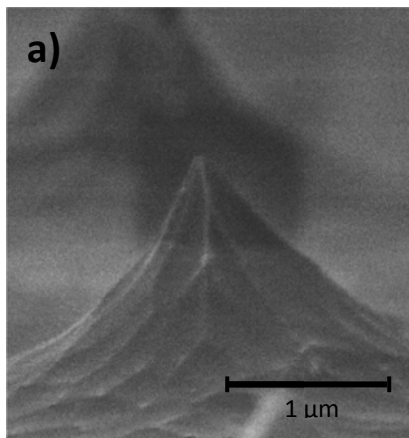Figure 6.2 SEM picture of a needle in 20 µm period a) before and b) after poling. The tip diameter increases from 50 nm to 500 nm during contacting silicon chip and crystal.

Besides the high pressure on each spike, the manual alignment is another reason for the broken spikes. Figure (6.3.a) illustrates a scratch on the c^+ face of the crystal which is caused by a sharp spike due to the manual alignment.
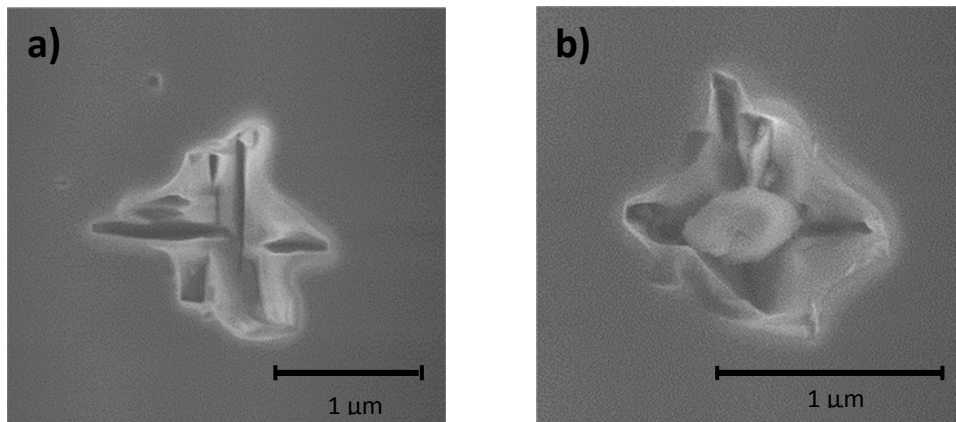
Figure 6.3 SEM pictures of scratches. (a) Scratch of one spike on the crystal surface after alignment. (b) Scratch and broken electrode tip (lying inside) on the RKTP crystal surface.

Extremely sharp spikes on the Si electrode surface can be another reason for the shape variation in the domains. A sharp spike can penetrate into the crystal surface and leaves thereby a trace in some of the domain areas. Figure (6.3.b) shows a possible broken Si spike tip inside a scratch on the crystal surface. The shape of electric field for such a sharp spike may lead to the ring shape domain. Ring-shaped domains feature a central part of the domain area where the polarization is not inverted.
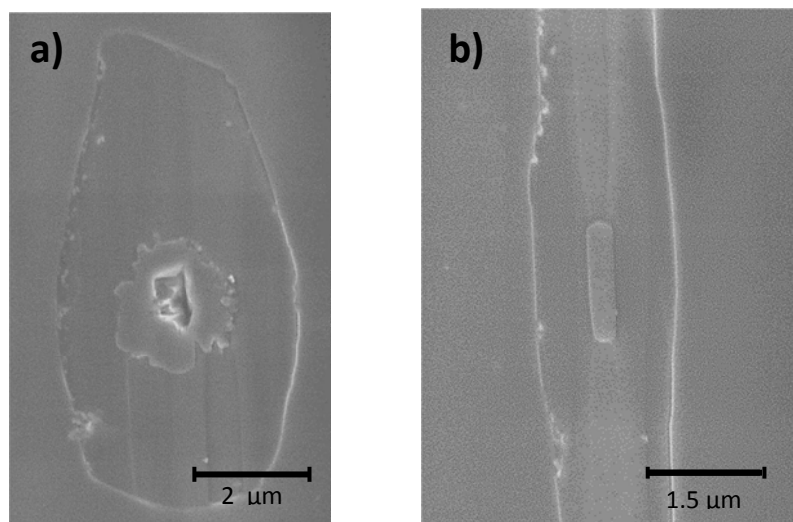
Figure 6.4 SEM pictures of domains formed by a sharp spike. (a) Outer dimension: 3 μm, inner not inverted area dimension: 1.5 μm, spike scratch dimension: 450 nm. (b) Not inverted area inside a domain without any scratch, width: 200 nm.

Figure (6.4.a) illustrates a ring-shaped domain with the scratch inside it in higher magnification. The ring shapes are also evident in the domains without scratch (Fig.(6.4.b)). Hence, it is probable that the formation of the ring shapes relies on the inhomogeneous electric field caused by very sharp spikes.

Figure (6.1) shows the domain structures of one particular RKTP sample for different parts of the crystal. There are 2D domain structures as well as elongated 2D domains and 1D domains on the c^+ polar face (Fig.(6.1.a), (6.1.c), (6.1.e)). Their corresponding domains on the c^- face are shown on the right hand side (Fig.(6.1.b), (6.1.d), (6.1.f)). In most of the domains on the c^+ face, ring-shaped and spike scratches can be observed.

Since the spike tip diameter is increased after the sample mounting, the fabricated domain dimensions are larger than what was anticipated. Due to the quasi-one dimensional structure of the RKTP, 2D domains tend to merge together in the b-direction and form a 1D domain structure. Therefore, in samples containing 2D domain structures, the fabricated domains are larger along the b-axis ($\sim$3.5 - 4.2 μm) and narrower along the a-axis ($\sim$2.4 - 3.8 μm). Their corresponding domains on the c^- polar face follows the same criteria. In samples with 1D domains on the c^+ polar face, the width of the domains in the a-direction is larger at the location of the spike contact ($\sim$4.1 μm) and narrower in between ($\sim$1.6 μm). The information regarding the domains dimensions in both polar faces are listed in Table (6.1). The reason for this is the high value of the fringing field around the spike tip and also the hard contact of the electrode and the crystal surface. The corresponding 1D domains on the c^- polar face are homogenous and have a width of 1.9 μm.

Domain type	2D	Elongated 2D	1D
Dimension in c^+	3.7 μm× 3.7 μm	3.8 μm×16.5 μm	1.6 & 4.1 μm
Dimension in c^-	1.5 μm × 3.7 μm	2.9 μm	1.9 μm

Table 6.1 Domain shape and dimension in Λ = 20 μm grating

6.1.2 Domain evaluation for 5 μm period grating

Six RKTP samples were poled with a 5 μm grating electrode. Grating patterns of 5 μm periods are successfully reproduced on the polar faces of the crystal by applying an electric field of 5.4 kV/mm with a triangular pulse of 5 ms duration.

Fabricated domain structures with a 5 μm period silicon electrode is more uniform across the crystal surface. Uniform domain structures come from the fact that the contact area of the crystal surface and the electrode is now more homogenous than in the Λ = 20 μm case. Several parameters lead to the uniform contact. First, all the plateaus on the silicon array of electrodes have the same height. Second, top areas of the plateaus are perfectly flat because they have the initial surface of the silicon wafer. Third, the density of the plateaus is high over the whole surface and this results in a total lower pressure on each individual needle electrode. Therefore, better domain grating quality is to be expected for the RKTP samples poled with Λ = 5 μm Si electrodes. However, the problem of the manual alignment and the pressing of the silicon array and crystal together still affects the poling process.

Figure 6.5 Domain structures of poled RKTP sample with 5.4 kV/mm triangular pulse of 3 ms duration and 5 µm grating length. (a) c^+ Domains dimension 2.5 × 4.1 µm (b) c^- Domains width 2.5 µm.

Figure 6.6 Domain structures of poled RKTP sample with 5.4 kV/mm triangular pulse of 3 ms duration and 5 µm grating length. (a) C^+ Domains dimension 2.5 × 3.8 µm (b) C^- Domains width 2.6 µm.

Due to the quasi-1D crystal structure of KTP, the domains tend to elongate in the b-direction. However, in the a-direction, domains on both the polar faces have fairly much the same dimensions. Fig.(6.5) and Fig.(6.6) show the domain structures of two different samples poled with an electric field of the same magnitude. The fabricated domains in these two samples have similar shapes and the dimensions and the domain structures are reproduced successfully.

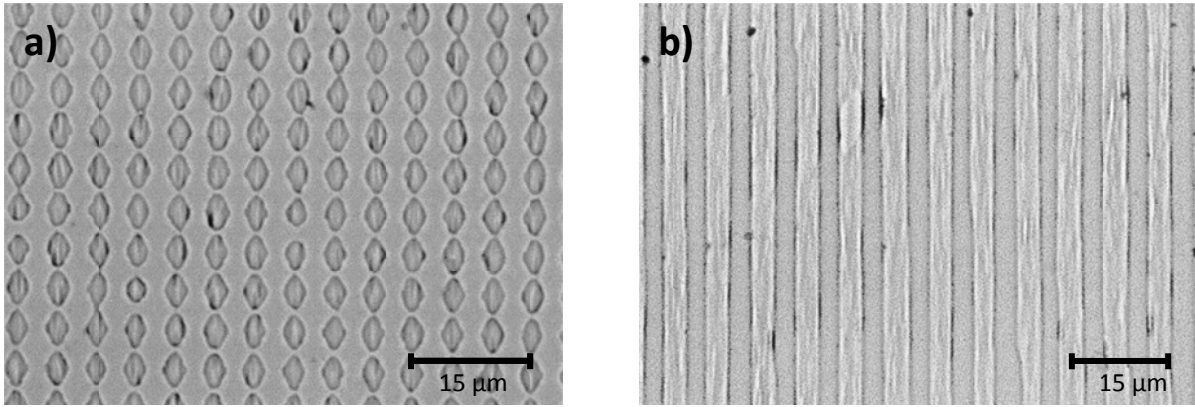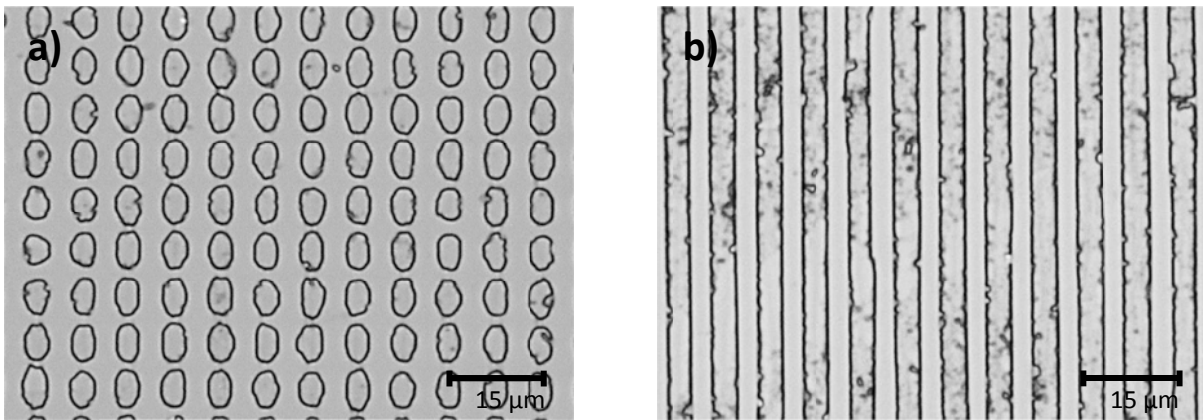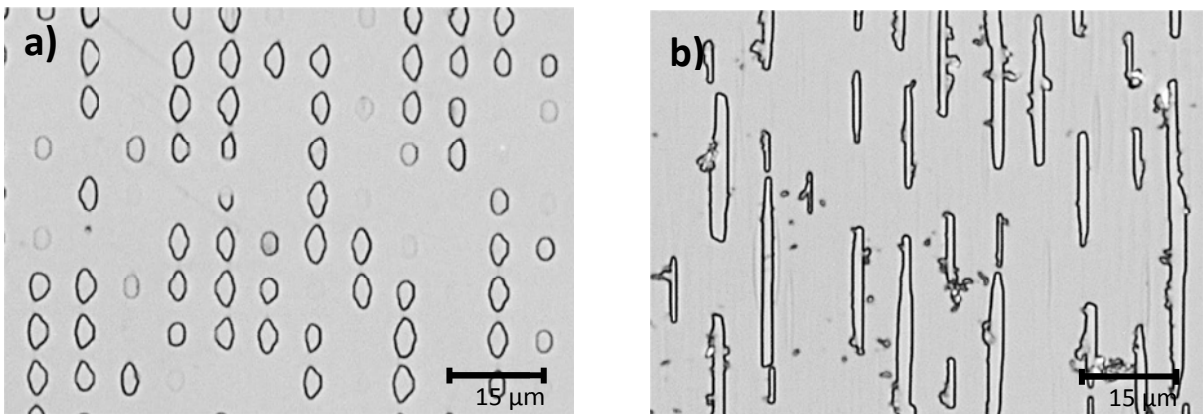*Figure 6.7 Domain structures of poled RKTP sample with 5 kV/mm triangular pulse of 3 ms duration and 5 µm grating length. (a) c^+ Domains dimension 2 × 3 µm (b) c^- Domains are distributed randomly width: 1 µm.*

On the other hand, inhomogeneous pressure, lower applied electric field, and lack of good alignment result in many missing domains as is shown in Fig.(6.7).

6.2 Optical characterization

The silicon spikes are very sharp for the 20 µm period electrodes. This results in a non-optimal duty cycle of the fabricated domain structures. 5th order SHG process in the domain structures with non-optimal duty cycle results in a very low SH signal. However, in the case of the 5 µm grating, since the duty cycle in this case is close to the ideal case of 50 %, the 1st order SHG process with a measurable signal power, is observed. In order to evaluate the quality of the fabricated gratings in the RKTP crystals, the optical performance of two of the samples with the Λ = 5 µm grating were investigated. The generated SH signal which was created in this experiment is close to c⁻polar face, corresponds to [1,0] reciprocal lattice vector (RLV). This RLV is equivalent to 1D grating.

6.2.1 Conversion efficiency

One way to check the poling quality is to observe the SH conversion efficiency of the poled crystal. For a Gaussian beam, the conversion efficiency is given by the following expression [41]:

$$\eta = \frac{P_{SH}}{P_F} = \left(\frac{2\omega_F^2 d_{eff}^2 k_F P_F}{\pi n_F^2 n_{SH} \varepsilon_0 c^3} \right) Lh(B, \xi). \quad (6.1)$$

According to Eq.(6.1), the SH conversion efficiency increases linearly with the fundamental power, P_F, and the crystal length L. The conversion efficiency measurement were done for the SHG of a Ti:Sapphire laser beam at 894 nm for two PPRKTP samples with 5 µm grating periods [22], [29]. Figure (6.8) shows the experimental setup.
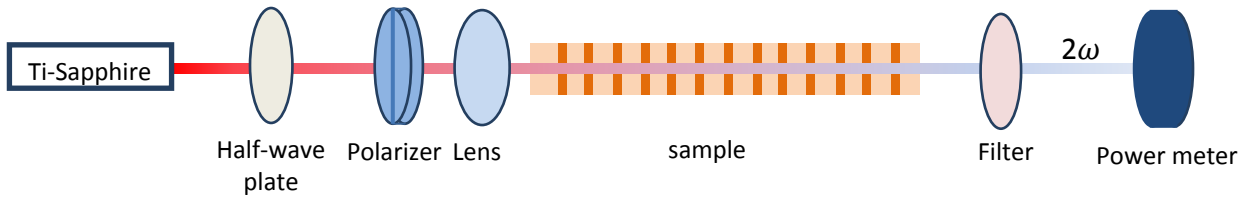

Figure 6.8 SHG setup for measuering conversion efficiency.

The measured efficiencies for these two samples are given in Fig.(6.9) and represent the efficiency of poling in 1D domain structure close to c⁻polar face. The experimental data of the conversion efficiencies fits very well with the linear theoretical function.
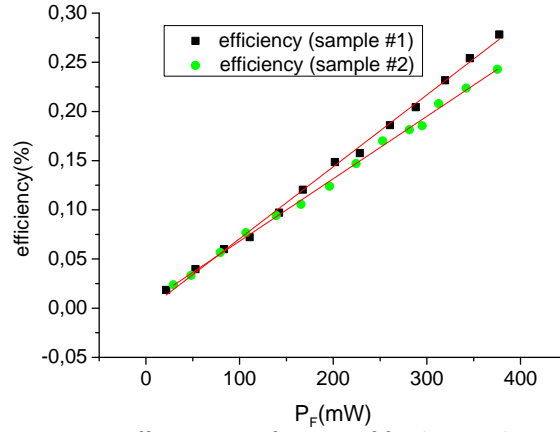
Figure 6.9 The SHG conversion efficiency as a function of fundamental power for 2 samples with 5 µm grating period. Circles and squares are measured data and red lines are linear fis, respectively.

In order to compare the conversion efficiency for the two different samples, it is common to use their normalized conversion efficiencies. The normalized conversion efficiency refers to an input of fundamental power of 1 Watt and a crystal length of 1 cm (with unit of %/Wcm). It is defined as follows:

$$\eta_{norm} = \frac{P_{SH}}{P^2{}_F L} = \left(\frac{2\omega_F^2 d_{eff}^2 k_F}{\pi n_F^2 n_{SH}\varepsilon_0 c^3}\right) h(B,\xi). \quad (6.2)$$

The maximum normalized conversion efficiency obtained for the best spot in sample #1 was 1.27 %/Wcm and 1.1 %/Wcm for sample #2. The generated SH powers were 1050 µW and 912 µW for an input power of 373 mW and 375 mW in sample #1 and #2 respectively. Based on Eq.(6.2), the SH power has a quadratic dependence on the fundamental power with a proportionality factor of $\eta_{norm}L$. Figure (6.10) below shows the SH signals dependence on the fundamental power. The experimental data agrees well with the theoretical fit.

Figure 6.10 The SH power versus the fundamental power in 2 different samples with 5 µm grating period. Solid squares and circles are experimental data and red solid line is the theorical curve.

6.2.2 Temperature acceptance bandwidth

The phase-matching phenomenon is sensitive to many parameters, such as the wavelength, temperature, and the polarization of the interacting waves. The acceptance bandwidth, also called the phase-matching tolerance, is defined as the relative change in the parameter that causes a drop of the output power to one half of the maximum value. In th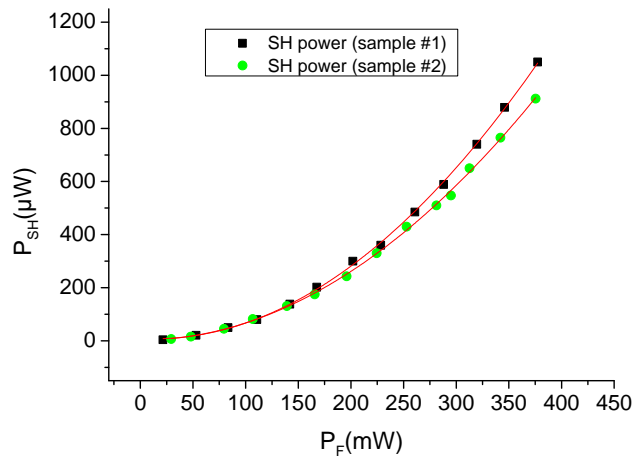is work, the temperature tuning characteristics of the SHG nonlinear interaction was investigated. For a fixed wavelength, the temperature bandwidth can be expressed as [16]:

$$\Delta T_{FWHM} = \frac{0.4429\lambda_\omega}{L} \left| \frac{\partial}{\partial T}(\Delta n) + \alpha \Delta n \right|, \qquad (6.3)$$

where α is the thermal expansion coefficient in the x-direction and Δn is the difference in the index of refraction. *L* is the length of the structure containing the uniform periodic ferroelectric domain grating.

    Temperature bandwidth measurement was performed for frequency doubling of a Ti:Sapphire laser at 894 nm. The setup is shown in Fig.(6.11) below and the measurement was done only for sample #2. The fundamental beam had 369 mW power and was polarized in the z-direction by a λ-half wave plate and a linear polarizer. The beam was focused by a lens into the crystal, close to the c⁻ polar face. A copper element was used together with a temperature controller (ILX Lightwave LDT-5525) in order to achieve the temperature tuning. The temperature in the copper element increased from 22 °C to 39 °C with 0.2 °C steps and the SH power was monitored at every step.

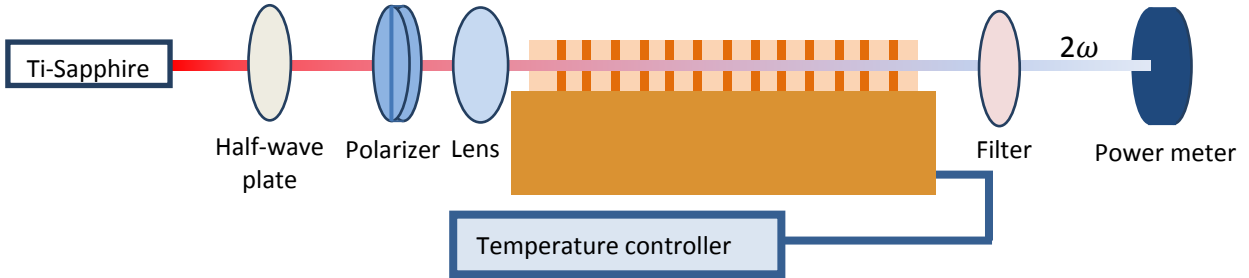*Figure 6.11 Temprature tuning setup for SHG.*

The temperature tuning curve obtained for the PPRKTP crystal with a period of 5 µm is shown in Fig.(6.12). The solid line is a theoretical function, which fits the experimental data well [42]. This confirms that a high-quality QPM structure in this crystal was obtained.
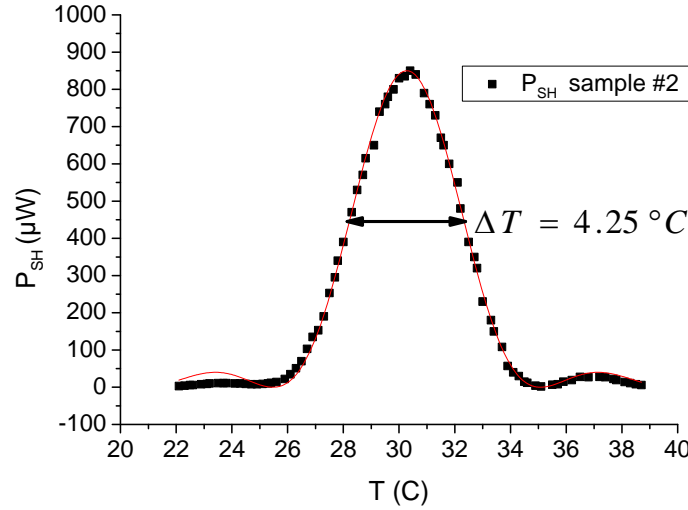
Figure 6.12 Temprature tuning curve for SHG, black squares show observed data and red line is the sinc^2 fitting funcion.

If the poling quality is low and there are missing domains in the structure, the effective interaction length of a periodically-poled crystal will be correspondingly reduced. According to Eq.(6.3), by measuring the bandwidth, the effective crystal length can be estimated as follows:

$$L_{eff} = \frac{0.4429\lambda_\omega}{\Delta T_{FWHM}} \left| \frac{\partial}{\partial T}(\Delta n) + \alpha \Delta n \right|. \qquad (6.4)$$

From the measured temperature bandwidth of 4.25 °C, the effective crystal length is estimated to be 5.4 mm. This value is very close to the physical grating length of 6 mm.

In this configuration, the QPM SHG process utilizes the d_{33} coefficient of the RKTP crystals, therefore, the effective nonlinear coefficient is related to the d_{33} in the following way [16]:

$$d_{eff} = \frac{2}{\pi} d_{33}.$$

The experimentally obtained nonlinear coefficient of our PPRKTP sample can be obtained from rearranging Eq.(6.2). Thus, the effective nonlinear coefficient is written as follows:

$$d_{eff} = \sqrt{\frac{\pi n_F^2 n_{SH} \varepsilon_0 c^3}{2\omega_F^2 k_F L h(B,\xi)} \times \frac{P_{SH}}{P^2_F}}. \qquad (6.5)$$

In order to evaluate the quality of the poled crystal, d_{eff} can be compared with the value, calculated using d_{33}, as taken from reference [43]. In our experiment, the RKTP crystal exhibits an effective nonlinear coefficient of 9.39 pm/V for a maximum output SH power of 896 µW. This value is close to the calculated value of $d_{eff} = 10.7$ pm/V for the first order SHG.

6.2.3 Domain merging point estimation

The fabricated domains with the 2D array of silicon electrode in the 5 µm periods are two-dimensional on the c^+ face of the crystal (where the electrode is in contact) and one-dimensional on the c^- polar face. Therefore, 2D domain structures merged along the b-axis during the propagation and became 1D on the non-contact face of the crystal. In order to find the exact position of the domain merging along the polar direction in the crystal, an SHG experiment was conducted in one of the PPRKTP crystals. The experimental setup is illustrated in Fig.(6.8) and was performed using the CW Ti:Sapphire laser lasing at a wavelength of 894 nm. Based on the concept which is explained in Section 2.7, the generated SH signal with this structure includes side peaks which represent more than one possible k-vector in a 2D QPM structure close to the c^+ face. When the Ti:Sapphire laser beam was scanned over the crystal thickness, the side peaks disappeared as soon as the 2D structure became 1D. The 2D domain structure merged and became a 1D ditto at a distance of 0.21 mm from the c^+ face.

7 Conclusions

In this work, a new method for fabrication of periodically-poled crystals is presented. This method is based on using an array of silicon spikes as an electrode for contact when performing electric-field poling of RKTP. The process for fabricating the silicon spikes is designed and subsequently optimized for different electrode shapes and formes. The final method is flexible, repeatable, and easy to modify for producing new types of electrodes with different sizes and geometries. The periodicity of the spikes ranges from 3.2 µm up to 20 µm. The process of producing spike array electrodes is overviewed in detail.

The constructed Si spike arrays are used as a 2D contact electrode for poling the RKTP with two different periodicities of 20 µm and 5 µm, respectively. Each individual silicon electrode on the final silicon array of electrodes has a conical shape in the 20 µm period case and a plateau shape in the 5 µm period case. The conical-shaped electrodes have very sharp spike tips resulting in a poorly controlled pressure in the poling cell employed. In the 20 µm period, the fabricated domains show pattern broadening. Nonetheless, the broadening can be reduced by mask modification and by improving the poling cell. The plateau-shaped electrodes produce domain structures which are similar to the fabricated domains using conventional technique. The domain broadening for the 5 µm period case has the same scale as that of the broadening with metal-deposited electrodes. However, it can be reduced by improving the poling cell and by controlling the pressure between the RKTP crystal and the silicon electrode. The domain broadening is also affected by the electrode geometry and can be adjusted by modifying the geometry of the plateau for different periods. Moreover, the fabricated domains for this period are reproduced by applying the same parameters for two different samples. To the best of our knowledge, this is the first time this technique has been used for fabricating periodically poled RKTP (PPRKTP).

The duty cycle of the fabricated domains for the 5 µm periods is close to the ideal case of 50 %. Therefore, the optical performance of the PPRKTP crystals with this period was further evaluated. Two samples poled with 5 µm period are used to generate second-harmonic (SH) signals and to investigate the conversion efficiency of the SH process for fabricating QPM devices. The normalized conversion efficiencies for these two samples are higher than 1 %/Wcm and, thus, this indicates good optical performance. The evaluated effective grating length from the measured temperature acceptance bandwidth is 5.4 mm, which is close to the physical grating length of 6 mm. Thus, the fabricated domains are uniformly structured demonstrating the high-quality poling obtained with this technique.

7.1 Further developments

There is a variety of interesting future experiments that can be done based on this work. They can be divided into two main categories: 1) modification of the silicon electrode structure and 2) more detailed investigation of the poling process.

It was observed that by using sharp spikes for the poling, resulted in non-uniform contact and non-homogenous ring-shaped domain structures. Therefore, in the case of silicon electrode modification, first, it is beneficial to polish the spike electrode and thereby reduce the sharpness. Second, the spikes and the plateaus can be fabricated with a larger height by introducing the Bosch process. An array of silicon spikes or plateaus with large height can be partially covered with a layer of photoresist resulting in a better isolation during the poling process. Third, in order to control the domain broadening, the geometry of the silicon spike and plateau electrodes can be modified. Reducing the electrode dimension in the b-direction could result in less domain broadening leading to a complete 2D domain structure on both the polar faces of the crystal. Forth, the electrode material can be changed to analyze the influence of different materials on poling. The p-type silicon electrode can be replaced by an n-type silicon or metalized polymer spikes. The fabrication of polymer spikes is flexible and well developed. Therefore, a metalized polymer array of spikes can serve as a good alternative electrode choice to the silicon spikes. Furthermore, modifiation of the electrode structure can be done in order to investigate the 1D periodic poling of KTP. In order to access this technique for fabricating domains in the nano-scale, silicon electrode specifications need to be modified.

Regarding the poling process itself, the following aspets can be improved upon. The poling cell should be upgraded so as to provide a better pressure and alignment control. The poling parameters such as the pulse shape, pulse duration and the number of pulses can be optimized. Thus, periodically-poled crystals with higher quality can be obtained.

8 References

[1]   G. Rosenman, D. Eger, and M. Katz, "Domain broadening in quasi-phase-matched nonlinear optical devices," *Applied Physics Letters*, vol. 73, no. 7, p. 865, 1998.

[2]   K. Kiantaka, M. Fujimura, T. Suhara, and H. Nishihara, "High-Efficiency LiNbO3 Waveguide Second-Harmonic Generation devices with Ferroelectric-Domain-Inverted Gratings Fabricate by Applying Voltage," *Light Wave Technology*, vol. 14, no. 3, 1996.

[3]   C. Canalias, V. Pasiskevicius, M. Fokine, and F. Laurell, "Backward quasi-phase-matched second-harmonic generation in submicrometer periodically poled flux-grown KTiOPO4," *Applied Physics Letters*, vol. 86, no. 18, p. 181105, 2005.

[4]   A. Zukauskas, G. Strömqvist, V. Pasiskevicius, F. Laurell, M. Fokine, and C. Canalias, "Fabrication of submicrometer quasi-phase-matched devices in KTP and RKTP," *Optical Materials Express*, vol. 1, no. 7, p. 1319, Oct. 2011.

[5]   C. Canalias and V. Pasiskevicius, "Mirrorless optical parametric oscillator," *Nature Photonics*, vol. 1, no. 8, pp. 459–462, Aug. 2007.

[6]   C. Canalias, V. Pasiskevicius, R. Clemens, and F. Laurell, "Submicron periodically poled flux-grown KTiOPO4," *Applied Physics Letters*, vol. 82, no. 24, p. 4233, 2003.

[7]   H. Kintaka, K, Fujimura, M, Suhara, T and Nishihara, "Fabrication of ferroelectric-domain-inverted grating in LiNbO3 by applying voltage using etched-Si stamper electrode," vol. 34, no. 9, pp. 2–3, 1998.

[8]   P. A. Franken, A. E. Hill, C. W. Peters, and G. Weinreich, "Generation of optical harmonics," *Physical Review Letters*, vol. 7, no. 1, pp. 118–120, 1961.

[9]   F. Träger and ..., *Springer Handbook of Lasers and Optics*. 2007, pp. 157–248.

[10]   S. Bahaa E. A., *Fundametal of Photonics*, no. born 1920. 1981, pp. 773–817.

[11]   R. C. Miller, "Optical second harmonic generation in piezoelectric crystals," *Applied Physics Letters*, vol. 5, p. 17, 1964.

[12]   R. W. Boyd, *Nonlinear Optics*, Third. AP, 2007, pp. 9–17.

[13]   L. E. Myers, R. C. Eckardt, M. M. Fejer, R. L. Byer, W. R. Bosenberg, and J. W. Pierce, "Quasi-phase-matched optical parametric oscillators in bulk periodically poled LiNbO_3," *Journal of the Optical Society of America B*, vol. 12, no. 11, p. 2102, Nov. 1995.

[14]   F. Laurell, "Periodically poled materials for miniature light sources," *Optical Materials*, vol. 11, no. January, pp. 235–244, 1999.

[15] H. Suchowski, B. D. Burner, A. Arie, and Y. Silberberg, "Broadband Nonlinear Frequency Conversion," *Optic and Photonic News*, pp. 36–41, 2010.

[16] M. M. Fejer, G. a. Magel, D. H. Jundt, and R. L. Byer, "Quasi-phase-matched second harmonic generation: tuning and tolerances," *IEEE Journal of Quantum Electronics*, vol. 28, no. 11, pp. 2631–2654, 1992.

[17] Y. Lu, Y. Lu, X. Cheng, G. Luo, C. Xue, and N. Ming, "Formation mechanism for ferroelectric domain structures in a LiNbO3 optical superlattice," *Applied Physics Letters*, vol. 68, no. 19, p. 2642, 1996.

[18] J. D. Bierlein, D. B. Laubacher, J. B. Brown, and C. J. van der Poel, "Balanced phase matching in segmented KTiOPO4 waveguides," *Applied Physics Letters*, vol. 56, no. 18, p. 1725, 1990.

[19] M. C. Gupta, W. P. Risk, A. C. G. Nutt, and S. D. Lau, "Domain inversion in KTiOPO4 using electron beam scanning," *Applied Physics Letters*, vol. 63, no. 9, p. 1167, 1993.

[20] H. Karlsson and F. Laurell, "Electric field poling of flux grown KTiOPO4," *Applied Physics Letters*, vol. 71, no. 24, p. 3474, 1997.

[21] V. Berger, "Nonlinear Photonic Crystals," *Physical Review Letters*, vol. 81, no. 19, pp. 4136–4139, Nov. 1998.

[22] C. Canalias, "Domain Engineering in KTP," Royal Institute of Technology, 2005.

[23] F. C. Zumsteg, J. D. Bierlein, and T. E. Gier, "KxRb1−xTiOPO4: A new nonlinear optical material," *Applied Physics*, vol. 47, p. 4980, 1976.

[24] C. Canalias, *Domain Engineering in*. 2005.

[25] S. Wang, "Fabrication and characterization of periodically-poled KTP and Rb-doped KTP for applications in the visible and UV," Royal Institute of Technology, 2005.

[26] J. D. Bierlein Company and F. Ahmed, "Observation and poling of ferroelectric domains in KTiOPO4," *Applied Physics Letters*, vol. 51, no. 17, p. 1322, 1987.

[27] Q. Jiang, P. A. Thomas, K. B. Hutton, and R. C. C. Ward, "Rb-doped potassium titanyl phosphate for periodic ferroelectric domain inversion," *Journal of Applied Physics*, vol. 92, no. 5, p. 2717, 2002.

[28] a. Fragemann, V. Pasiskevicius, J. Nordborg, J. Hellström, H. Karlsson, and F. Laurell, "Frequency converters from visible to mid-infrared with periodically poled RbTiOPO[sub 4]," *Applied Physics Letters*, vol. 83, no. 15, p. 3090, 2003.

[29] S. Wang, V. Pasiskevicius, and F. Laurell, "High-efficiency frequency converters with periodically-poled Rb-doped KTiOPO4," *Optical Materials*, vol. 30, no. 4, pp. 594–599, Dec. 2007.

[30] C. Canalias, S. Wang, V. Pasiskevicius, and F. Laurell, "Nucleation and growth of periodic domains during electric field poling in flux-grown KTiOPO[sub 4] observed by atomic force microscopy," *Applied Physics Letters*, vol. 88, no. 3, p. 032905, 2006.

[31] C. Canalias, J. Hirohashi, V. Pasiskevicius, and F. Laurell, "Polarization-switching characteristics of flux-grown KTiOPO4 and RbTiOPO4 at room temperature," *Journal of Applied Physics*, vol. 97, no. 12, p. 124105, 2005.

[32] N. Roxhed, "A fully integrated microneedle-based transdermal drug delivery system," Royal Institute of Technology, 2007.

[33] W. Trimmer, P. Ling, C. Chin, P. Orton, B. Brunett, M. Reed, R. Gaugler, S. Hashmi, and G. Hashmi, "Injection of DNA into plant and animal Tissues with micromechanical piercing structures," *IEEE*, vol. 2, pp. 111–115, 1995.

[34] D. . McAllister, F. Cros, S. P. Davis, L. M. Matta, M. R. Prausnitz, and M. G. Allen, "Three-dimensional hollow microneedle and microtube arrays," in *The 10th Int. Conf. on Solid-state Sensors and Actuators*, 1999, pp. 1098–101.

[35] S. Henry, D. V. McAllister, M. G. Allen, and M. R. Prausnitz, "Microfabricated microneedles: A novel approach to transdermal drug delivery," *Journal of pharmaceutical sciences*, vol. 88, no. 9, p. 948, Sep. 1999.

[36] B. Stoeber and D. Liepmann, "Arrays of hollow out-of-plane microneedles for drug delivery," *Journal of Microelectromechanical Systems*, vol. 14, no. 3, pp. 472–479, Jun. 2005.

[37] N. Roxhed, T. C. Gasser, P. Griss, G. A. Holzapfel, and G. Stemme, "Penetration-Enhanced Ultrasharp Microneedles and Prediction on Skin Interaction for Efficient Transdermal Drug Delivery," *Journal of Microelectromechanical Systems*, vol. 16, no. 6, pp. 1429–1440, Dec. 2007.

[38] J. D. Plummer, M. D. Deal, and P. B. Griffin, *Silicon VLSI Technology*. Prentice Hall, 2000.

[39] H. Karlsson, F. Laurell, and L. K. Cheng, "Periodic poling of RbTiOPO4 for quasi-phase matched blue light generation," *Applied Physics Letters*, vol. 74, no. 11, p. 1519, 1999.

[40] F. Laurell, M. G. Roelofs, W. Bindloss, H. Hsiung, A. Suna, and J. D. Bierlein, "Detection of ferroelectric domain reversal in KTiOP4 waveguides," *Journal of Applied Physics*, vol. 71, no. 10, p. 4664, 1992.

[41] G. D. Boyd, "Parametric Interaction of Focused Gaussian Light Beams," *Journal of Applied Physics*, vol. 39, no. 8, p. 3597, 1968.

[42] W. Wiechmann, S. Kubota, T. Fukui, and H. Masuda, "Refractive-index temperature derivatives of potassium titanyl phosphate.," *Optics letters*, vol. 18, no. 15, pp. 1208–10, Aug. 1993.

[43] H. Vanherzeele and J. D. Bierlein, "Magnitude of the nonlinear-optical coefficients of KTiOPO4.," *Optics letters*, vol. 17, no. 14, pp. 982–4, Jul. 1992.